

Gaussian Blending: Rethinking Alpha Blending in 3D Gaussian Splatting

Junseo Koo, Jinseo Jeong, Gunhee Kim

Seoul National University

junseo.koo@vision.snu.ac.kr, jinseo.jeong@vision.snu.ac.kr, gunhee@snu.ac.kr
<https://1207koo.github.io/html/gaussianblending/>

Abstract

The recent introduction of 3D Gaussian Splatting (3DGS) has significantly advanced novel view synthesis. Several studies have further improved the rendering quality of 3DGS, yet they still exhibit noticeable visual discrepancies when synthesizing views at sampling rates unseen during training. Specifically, they suffer from (i) erosion-induced blurring artifacts when zooming in and (ii) dilation-induced staircase artifacts when zooming out. We speculate that these artifacts arise from the fundamental limitation of the alpha blending adopted in 3DGS methods. Instead of the conventional alpha blending that computes alpha and transmittance as scalar quantities over a pixel, we propose to replace it with our novel *Gaussian Blending* that treats alpha and transmittance as spatially varying distributions. Thus, transmittances can be updated considering the spatial distribution of alpha values across the pixel area, allowing nearby background splats to contribute to the final rendering. Our Gaussian Blending maintains real-time rendering speed and requires no additional memory cost, while being easily integrated as a drop-in replacement into existing 3DGS-based or other NVS frameworks. Extensive experiments demonstrate that Gaussian Blending effectively captures fine details at various sampling rates unseen during training, consistently outperforming existing novel view synthesis models across both unseen and seen sampling rates.

1 Introduction

Novel view synthesis (NVS) has advanced rapidly, playing a pivotal role across diverse content generation tasks. A key milestone was Neural Radiance Field (NeRF) (Mildenhall et al. 2021), an implicit neural representation employing a neural network to estimate volumetric density and view-dependent radiance of 3D points. However, NeRF suffers from slow rendering speeds due to intensive ray marching. Recently, 3D Gaussian Splatting (3DGS) (Kerbl et al. 2023) explicitly represents 3D scenes using Gaussian splats, enabling faster and finer view synthesis results.

In the 3DGS framework, Gaussian splats are projected onto the 2D image plane, followed by the alpha blending to render the final pixel color. However, 3DGS and its variants still suffer from noticeable artifacts when synthesizing views at unseen sampling rates (e.g., zoom-in or zoom-out).

Copyright © 2026, Association for the Advancement of Artificial Intelligence (www.aaai.org). All rights reserved.

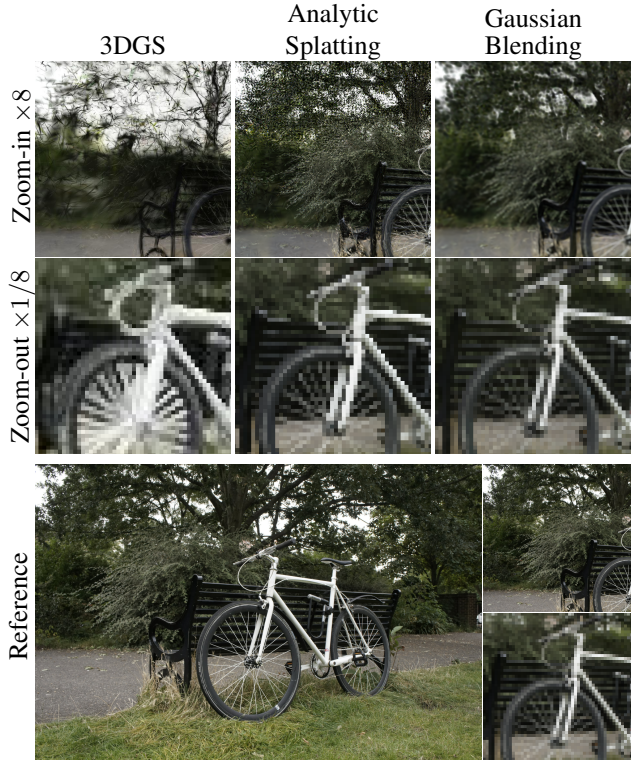


Figure 1: Scalar alpha blending used in previous novel view synthesis methods (e.g., 3DGS and Analytic Splatting) exhibits aliasing artifacts when rendering at different sampling rates. Specifically, erosion with noisy edges occurs during zoom-in (top), while dilation with staircase artifacts occurs during zoom-out (bottom). In contrast, our Gaussian Blending produces consistent synthesis results at unseen sampling rates (e.g., leaves and bicycle frame) without any priors and additional training.

This persistent challenge arises since existing methods treat pixels as points rather than planes, which leads to aliasing effects such as boundary erosion and dilation (see Figure 1).

In real-world camera systems, a sensor integrates radiances within a pixel area, whereas existing NVS methods use single ray for rendering a pixel color. According to the

Nyquist–Shannon sampling theorem (Shannon 1949), suppressing high-frequency components at lower sampling rates can alleviate this issue, as supported by several prefiltering methods (Barron et al. 2021, 2022; Yu et al. 2024b). More recently, Analytic-Splatting (Liang et al. 2024b) explicitly integrates Gaussian splat responses over pixel regions, better emulating physical camera sensors.

Despite recent advances, existing NVS approaches still exhibit noticeable aliasing, especially at object boundaries. As illustrated in Figure 1, rendering at higher sampling rates (zoom-in) produces boundary erosion with blurry edges, while lower sampling rates (zoom-out) produce boundary dilation as staircase artifacts. Even Analytic-Splatting suffers from these issues due to reliance on scalar alpha blending. All NVS methods, including various anti-aliasing methods, use scalar alpha values computed along single rays. This inherently leads foreground splats (or density points in NeRF-based methods) to fully occlude background splats, disregarding their spatial overlap in the 2D screen space. Consequently, the spatial contribution of background splats is inaccurately computed, causing persistent aliasing. To mitigate this issue, existing NVS methods typically require retraining models at specific sampling rates, which is inefficient and impractical when training data are unavailable.

To address this limitation, we introduce *Gaussian Blending* as a novel rendering methodology. Rather than modeling alpha and transmittance as single scalar values, our approach models them as spatially varying functions across the 2D pixel area. Our key insight is that Gaussian splats, being smooth and continuous, naturally cluster to represent distinct scene structures. Leveraging this spatial coherence, we approximate their combined transmittance using simplified 2D uniform distributions within each pixel region. This approximation enables efficient, dynamic updating of spatial transmittance distributions during the alpha blending process via distributional moments.

In experiments on the multi-scale Blender (Mildenhall et al. 2021; Barron et al. 2021) and Mip-NeRF 360 datasets (Barron et al. 2022), Gaussian Blending significantly reduces intra-pixel aliasing, mitigating erosion and dilation at previously unseen sampling rates. Moreover, Gaussian Blending achieves real-time rendering speeds comparable to the original 3DGS method via optimized CUDA implementation, improving visual fidelity without extra memory overhead. In addition, it can be seamlessly integrated as a drop-in replacement for the rendering kernels of existing NVS frameworks.

Finally, our key contributions are as follows.

- We revisit existing scalar alpha blending methods and identify that aliasing arises from inadequate handling of the spatial variations within pixel regions.
- To the best of our knowledge, our work is the first to integrate intra-pixel anti-aliasing into the alpha blending process explicitly. Our proposed *Gaussian Blending* efficiently models and dynamically tracks spatial variations within pixels to effectively suppress aliasing.
- Extensive experiments demonstrate that Gaussian Blending significantly reduces aliasing, yielding higher-quality

synthesized views at both unseen and seen sampling rates during training, without additional priors or retraining, all while preserving real-time performance. Our Gaussian Blending can be easily integrated as a drop-in replacement into existing NVS frameworks.

2 Related Work

2.1 Novel View Synthesis (NVS)

NVS aims to reconstruct the geometry and appearance of 3D scenes from multi-view images, enabling rendering from unseen viewpoints (Pumarola et al. 2021; Park et al. 2021; Yang et al. 2024; Jeong et al. 2024; Liang et al. 2024a; Moenne-Loccoz et al. 2024). While Neural Radiance Fields (NeRF) (Mildenhall et al. 2021) have laid the groundwork, they suffer from slow rendering speeds due to intensive ray marching. To overcome these limitations, subsequent methods adopt explicit grid-based scene representations (Sun, Sun, and Chen 2022; Chen et al. 2022), significantly enhancing rendering efficiency through strategies like free-space skipping. Hybrid methods further combine NeRF with Signed Distance Functions (SDF) (Wang et al. 2021; Wu et al. 2023), extending implicit representations to support accurate surface reconstruction.

3D Gaussian Splatting (3DGS) (Kerbl et al. 2023) represents scenes as collections of Gaussian splats, enabling real-time, high-quality rendering. Unlike implicit neural methods involving computationally heavy ray marching, 3DGS rasterizes Gaussian splats directly into screen space, allowing efficient rendering via GPU-optimized rasterization with explicit alpha blending. Building upon this framework, several variants have been proposed to further enhance rendering quality and efficiency. 2D Gaussian Splatting (2DGS) (Huang et al. 2024) and 3D Half-Gaussian Splatting (3D-HGS) (Li et al. 2025) respectively introduce 2D Gaussian splats and half-Gaussian kernels, to better capture geometric details. Scaffold-GS and Octree-GS (Lu et al. 2024; Ren et al. 2024) employ anchor-based or Level-of-Detail-structured 3D Gaussians to reduce redundancy and enhance efficiency in large-scale view-varying scenarios. These advances have broadened the applicability of NVS, including dynamic scene reconstruction (Pumarola et al. 2021; Park et al. 2021; Yang et al. 2024), generative modeling (Poole et al. 2023; Haque et al. 2023; Lin et al. 2025), and inverse rendering tasks (Jeong et al. 2024; Liang et al. 2024a; Moenne-Loccoz et al. 2024), inspiring numerous downstream developments.

2.2 NVS at Different Sampling Rates

Despite rapid progress in NVS, most existing methods assume fixed resolutions, camera distances, and camera intrinsics. However, real-world applications often involve varying sampling rates, causing noticeable aliasing artifacts due to single ray rendering that neglects the visible frustum.

Several methods have addressed this issue through prefiltering-based anti-aliasing approaches following the Nyquist–Shannon Sampling Theorem (Shannon 1949). For example, Mip-NeRF (Barron et al. 2021) reduces aliasing by

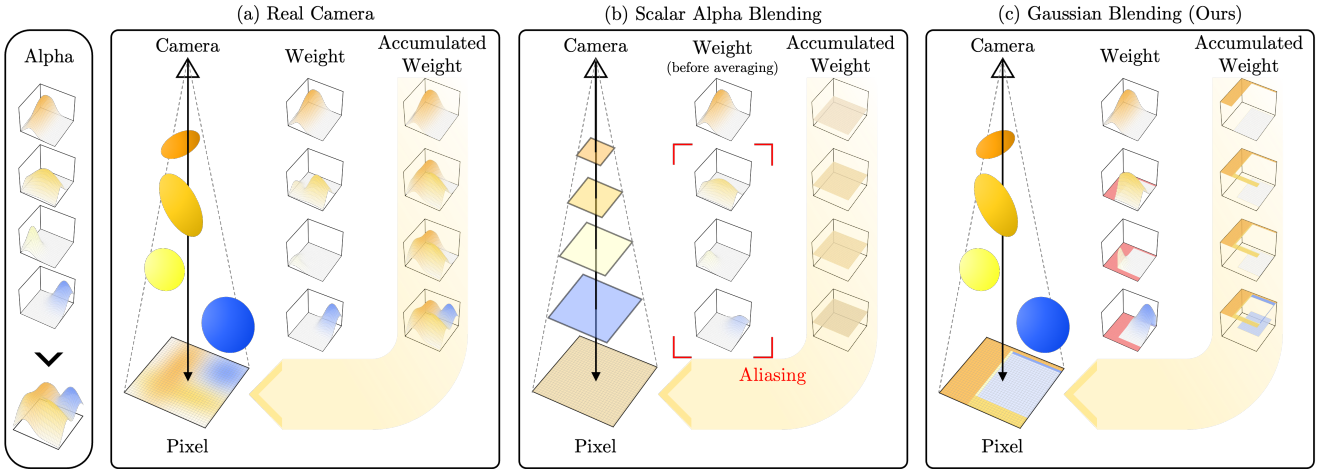


Figure 2: Comparison of blending behaviors when rendering overlapping splats. (a) In a real camera system, spatial occlusion is properly handled—the yellow splat is attenuated by closer splats, while the blue splat, which does not overlap in screen space, retains high transmittance and remains visible. (b) Scalar alpha blending ignores spatial occlusion by averaging alpha values across the pixel, causing dilation of the overlapping yellow splat and undesired suppression of the non-overlapping blue splat. (c) Our Gaussian Blending dynamically adjusts the transmittance window within each pixel, preserving high transmittance in regions without splats and effectively maintaining the visibility of the blue splat while reducing the influence of the occluded yellow splat.

integrating positional encoding over spatial regions, effectively applying implicit low-pass filtering. Mip-NeRF 360 (Barron et al. 2022) further extends this approach to handle unbounded scenes, addressing aliasing more effectively in realistic scenarios. With the emergence of 3DGS, Mip-Splatting (Yu et al. 2024b) combines 2D and 3D filtering strategies, mitigating dilation artifacts caused by varying sampling rates. Going beyond these filtering-based approaches, Analytic-Splatting (Liang et al. 2024b) analytically computes Gaussian splat responses over pixel areas, explicitly integrating splat contributions to achieve effective and accurate anti-aliasing.

Mipmap-based approach is another popular strategy to handle anti-aliasing. They often train separate scene representations for each sampling rate. Instant-NGP (Müller et al. 2022) pioneers resolution-adaptive rendering through multi-resolution hash-grid features. Tri-MipRF (Hu et al. 2023) introduces learnable mipmap representations, dynamically retrieving resolution-specific features during rendering. Recent adaptations (Li et al. 2024; Yan et al. 2024) group Gaussian splats based on sampling rates. However, these mipmap-based approaches can only handle specific resolutions seen during training, limiting their generalization.

Additionally, several studies focus on enhancing high-frequency details or resolving artifacts when rendering at higher sampling rates beyond training conditions. While straightforward techniques such as supersampling show limited effectiveness (Wang et al. 2022), recent approaches leverage generative diffusion models (Yu et al. 2024a; Xia and Liu 2025) or single-image super-resolution (SISR) frameworks (Feng et al. 2024) to generate pseudo-ground-truth details of test-time resolutions. Unlike these methods that improve image quality by generating high-frequency

details, our approach directly addresses aliasing artifacts caused by scalar alpha blending.

3 Approach

3.1 Preliminaries

3D Gaussian Splatting (3DGS) (Kerbl et al. 2023) explicitly represents a 3D scene using a set of Gaussian splats. Given a total of N splats, the i -th closest splat to the camera is parameterized by its center position $\mu_i \in \mathbb{R}^3$, scale vector $s_i \in \mathbb{R}^3$, rotation quaternion $r_i \in \mathbb{R}^4$, and opacity value $o_i \in \mathbb{R}$. The scale vector s_i forms a diagonal scale matrix $S_i \in \mathbb{R}^{3 \times 3}$, and the quaternion r_i defines a rotation matrix $R_i \in \mathbb{R}^{3 \times 3}$. Consequently, the 3D covariance matrix of the Gaussian splat is computed as

$$\Sigma_i = R_i S_i S_i^\top R_i^\top. \quad (1)$$

The influence of the i -th Gaussian splat at a 3D position x is defined as

$$G_i(x) = o_i \exp\left(-\frac{1}{2}(x - \mu_i)^\top \Sigma_i^{-1}(x - \mu_i)\right). \quad (2)$$

Each 3D Gaussian splat is projected onto the 2D screen space, resulting in the corresponding 2D Gaussian splat. Given a camera extrinsic matrix W and an intrinsic projection matrix K , the projected mean vector and covariance matrix are

$$\mu'_i = KW[\mu_i, 1]^\top, \quad \Sigma'_i = J_i W \Sigma_i W^\top J_i^\top, \quad (3)$$

where J_i is the Jacobian of the local affine approximation of the perspective projection at μ_i . By removing its third row and column, Σ'_i becomes a 2D covariance matrix in $\mathbb{R}^{2 \times 2}$.

Thus, the screen space influence of the projected Gaussian splat at a 2D position x is

$$G'_i(x) = o_i \exp\left(-\frac{1}{2}(x - \mu'_i)^\top \Sigma_i'^{-1}(x - \mu'_i)\right). \quad (4)$$

Given a pixel center p , each splat's alpha value is computed as the Gaussian influence evaluated at the pixel center $G'_i(p)$. Rendering is performed by blending these splats in the front-to-back depth order using alpha blending. As c_i is the view-dependent color of the i -th splat, the final pixel color C_p is computed as

$$C_p = \sum_{i=1}^N c_i G'_i(p) T_i, \quad T_i = \prod_{j=1}^{i-1} (1 - G'_j(p)), \quad (5)$$

where the contribution of each splat can be interpreted as the weight $w_i = G'_i(p) T_i$.

Analytic-Splatting (Liang et al. 2024b) extends the 3DGS approach by incorporating anti-aliasing through analytic integration of each Gaussian splat's influence over the entire pixel area, rather than evaluating it only at the pixel center. This integral of 2D Gaussian cannot be simplified with a closed form; thus, Analytic-Splatting employs an efficient approximation, which performs an eigen-decomposition on each 2D Gaussian splat to identify principal axes. Then, the pixel coordinate frame is rotated to align with these axes, eliminating the correlation term in the Gaussian function. Consequently, the integral can be factorized into two separable 1D Gaussian integrals along these axes, each computed analytically. Further details can be found in the original papers (Kerbl et al. 2023; Liang et al. 2024b).

3.2 Scalar Alpha Blending

Although Analytic-Splatting theoretically eliminates aliasing artifacts, as illustrated in Figure 1, it still exhibits persistent aliasing issues like erosion and dilation. We identify that these problems fundamentally originate from scalar alpha blending, and subsequently describe how our proposed approach overcomes this limitation.

Alpha blending is a fundamental rendering technique used by most NVS methods, including anti-aliasing approaches. However, conventional alpha blending represents alpha and transmittance as scalar values, ignoring critical spatial variations within pixels.

Physically, rendering should involve integrating spatially varying alpha and color distributions over each pixel region. The physically correct pixel color C_p^p is computed by integrating the contributions of all splats and resulting transmittance T_i^p within the pixel area p :

$$C_p^p = \int_p \sum_{i=1}^N T_i^p(x) \alpha_i(x) c_i dx, \\ T_i^p(x) = \prod_{j=1}^{i-1} (1 - \alpha_j(x)). \quad (6)$$

Existing methods approximate this integration by computing scalar alpha integrals independently for each splat:

$$C_p^s = \sum_{i=1}^N T_i^s c_i \int_p \alpha_i(x) dx, \\ T_i^s = \prod_{j=1}^{i-1} \left(1 - \int_p \alpha_j(x) dx\right), \quad (7)$$

where C_p^s is the approximated pixel color, and T_i^s is the scalar transmittance after rendering the i -th splat.

Figure 2 illustrates that such scalar approximations inevitably lead to aliasing artifacts. In a real camera system, overlapping splats that lie behind other splats should attenuate their alpha values due to spatial occlusion. However, the scalar approximation in alpha and transmittance ignores the spatial context such as occlusions, computing alpha values regardless of the spatial occlusion. This results in the object edges, which partially overlap within the pixel area, being rendered with higher alpha values than they should be, even though object splats are highly occluding each other. This rapidly saturates transmittance, leading to pixel-level dilation artifacts, where foreground objects appear artificially enlarged, and background objects (e.g., the blue splat in Figure 2) become overly occluded, as shown in Figure 1. At lower sampling rates (zoom-out), saturated transmittance causes dilation artifacts, despite the broader visible frustum per pixel. Conversely, at higher sampling rates (zoom-in), scalar alpha blending induces erosion artifacts with blurry boundaries due to dilation bias learned during training.

This limitation persists across all existing NVS approaches, including standard rendering, and prefiltering or mipmap-based anti-aliasing, since all rely on scalar alpha blending. Only supersampling approaches, which explicitly compute spatial variations in alpha and transmittance, accurately capture these effects. However, supersampling is computationally expensive, requiring multiple rendering passes, and is thus challenging to employ in real-time applications.

3.3 Efficient Spatial Alpha Blending

A straightforward and physically accurate approach to spatial variations in transmittance is to integrate the transmittance T_i and the corresponding weight w_i across each pixel's 2D screen space coverage. However, computing these integrals requires exponential computational complexity, as the transmittance $T_i = \prod_{j=1}^{i-1} (1 - \alpha_j)$ and the weight $w_i = \alpha_i T_i$ consist of $2^{i-1} - 1$ and 2^{i-1} terms, respectively.

Our key insight to mitigate this computational challenge is that Gaussian splats collectively represent continuous object surfaces, typically forming uniform alpha distributions across 2D screen space, such as $\alpha = 1$ for opaque surfaces. Thus, despite the transmittance involving an exponentially large number of Gaussian terms, these terms spatially cluster into compact regions, effectively approximated by a uniform distribution within each pixel area. Leveraging this observation, we approximate the transmittance distribution using a simpler, spatially uniform 2D representation.

By adaptively controlling the spatial extent of this uniform distribution, we dynamically modulate the effective

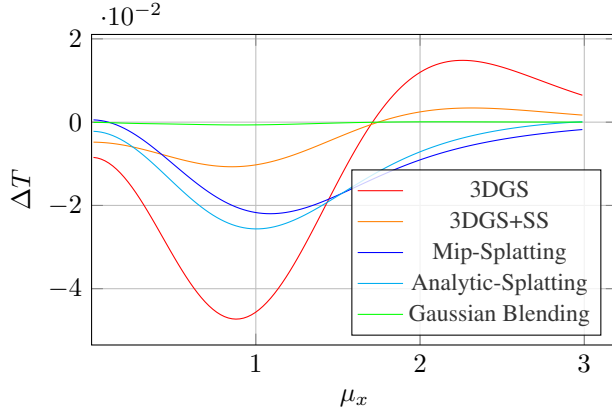


Figure 3: Comparison of the remaining transmittance error ΔT after rendering two splats symmetrically placed at $\mu_1 = [\mu_x, -0.1]^\top$ and $\mu_2 = [\mu_x, 0.1]^\top$, with $o_1 = o_2 = 1$ and $\sigma_1 = \sigma_2 = \sigma$. (**Left**) Varying μ_x while fixing $\sigma = 1$. (**Right**) Varying σ while fixing $\mu_x = 0.5$. A negative ΔT indicates dilation, where a lower transmittance remains after rendering.

transmittance, reducing the influence of splats located in regions already occluded by previously rendered surfaces, where transmittance values are low. This approach enables real-time rendering without compromising visual accuracy.

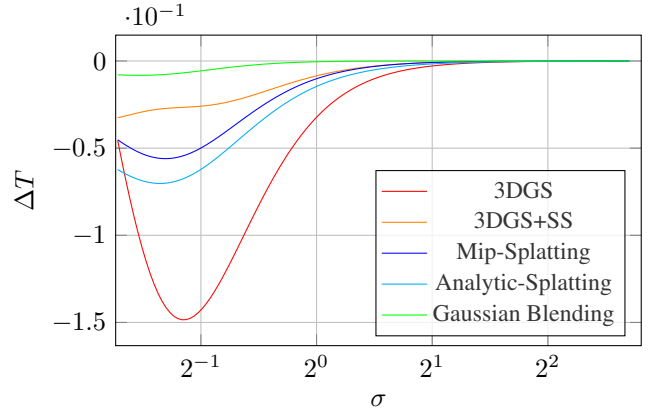
Moreover, representing transmittance as a 2D uniform distribution offers two physical advantages. First, it inherently satisfies $0 \leq w_i \leq T_i$ throughout the pixel, ensuring physically consistent blending. Second, the initial pixel state naturally conforms to a uniform distribution, simplifying the computation of subsequent rendering windows.

Formally, we represent transmittance T_i by a window centered at $x_i \in \mathbb{R}^2$ with size $l_i = [l_{i,1}, l_{i,2}]^\top \in \mathbb{R}^2$ and uniform transmittance value $t_i \in \mathbb{R}$. Initially, before any splats are rendered, T_1 is defined as $x_1 = p$, $l_1 = [1, 1]^\top$, and $t_1 = 1$. Assuming splats composing an object form uniform distributions in the pixel region, dynamically adjusting the window (x_i, l_i) enables accurate representation of lower-transmittance subregions.

When rendering splat α_i onto distribution T_i , we compute two quantities: (i) the integrated splat response within the current window region, $\int w_i(x)dx$, and (ii) the optimal distribution T_{i+1} approximating the remaining transmittance $T_i(x)(1 - \alpha_i(x))$.

Weight Computation. To compute a splat's response $\int w_i(x)dx$, we first perform eigen-decomposition on the 2D covariance matrix Σ'_i , yielding eigenvalues λ_1, λ_2 and unit eigenvectors e_1, e_2 , defining principal axes. The standard deviations along these axes are $\sigma_1 = \sqrt{\lambda_1}$ and $\sigma_2 = \sqrt{\lambda_2}$. Next, we rotate the current window T_i slightly (within 45°) to align it with the Gaussian axes defined by e_1, e_2 to efficiently approximate the integral. Without loss of generality, let us assume λ_1, e_1 align with the first axis, and λ_2, e_2 with the second axis. In the coordinate system defined by the splat α_i , centered at μ'_i , the window center is located at $[u, v]^\top = [(x_i - \mu'_i) \cdot e_1, (x_i - \mu'_i) \cdot e_2]^\top$, and the window region spans $[u_1, u_2] \times [v_1, v_2]$ with boundaries:

$$\begin{bmatrix} u_1 \\ v_1 \end{bmatrix} = \begin{bmatrix} u \\ v \end{bmatrix} - \frac{1}{2}l_i, \quad \begin{bmatrix} u_2 \\ v_2 \end{bmatrix} = \begin{bmatrix} u \\ v \end{bmatrix} + \frac{1}{2}l_i. \quad (8)$$



To simplify the integrals, we introduce the notation for the k -th order moments of the 1D Gaussian as $I_\sigma^k(a, b) = \int_a^b x^k \exp(-x^2/2\sigma^2)dx$. Then, we express the integrated weight as

$$\int w_i(x)dx = t_i o_i I_{\sigma_1}^0(u_1, u_2) I_{\sigma_2}^0(v_1, v_2). \quad (9)$$

Transmittance Computation. Next, we compute the optimal distribution T_{i+1} to approximate the remaining transmittance, $T_i(x)(1 - \alpha_i(x))$, after blending the current splat. Specifically, we calculate the zeroth-, first-, and second-order moments (M_i^0, M_i^1, M_i^2) of the resulting distribution within the current window to preserve the total transmittance mass, mean, and variance after each blending step. They are computed in the rotated coordinate system aligned with the splat's principal axes by

$$\begin{aligned} M_i^0 &= t_i l_{i,1} l_{i,2} - \int w_i(x)dx, \\ M_i^1 &= t_i l_{i,1} l_{i,2} \begin{bmatrix} u \\ v \end{bmatrix} - t_i o_i \left[\frac{I_{\sigma_1}^1(u_1, u_2) \cdot I_{\sigma_2}^0(v_1, v_2)}{I_{\sigma_1}^0(u_1, u_2) \cdot I_{\sigma_2}^1(v_1, v_2)} \right], \\ M_i^2 &= t_i l_{i,1} l_{i,2} \left(\begin{bmatrix} u^2 \\ v^2 \end{bmatrix} + \frac{1}{12} l_i^2 \right) \\ &\quad - t_i o_i \left[\frac{I_{\sigma_1}^2(u_1, u_2) \cdot I_{\sigma_2}^0(v_1, v_2)}{I_{\sigma_1}^0(u_1, u_2) \cdot I_{\sigma_2}^2(v_1, v_2)} \right]. \end{aligned} \quad (10)$$

Using these moments, we obtain the parameters of the new 2D uniform transmittance distribution T_{i+1} as

$$\begin{aligned} x_{i+1} &= \mu'_i + [e_1, e_2] M_i^1 / M_i^0, \\ l_{i+1} &= \sqrt{12 \left(M_i^2 / M_i^0 - (M_i^1 / M_i^0)^2 \right)}, \\ t_{i+1} &= M_i^0 / l_{i+1,1} l_{i+1,2}. \end{aligned} \quad (11)$$

Through this process, starting from an initially fully visible pixel area, we iteratively integrate the response of each splat and dynamically update the rendering window as in

Table 1: Single-scale training ($\times 1$ resolution) and multi-scale testing results on the multi-scale Blender dataset. The best results are highlighted in **bold**.

	$\times 1$	$\times 1/2$	$\times 1/4$	$\times 1/8$	Avg.	$\times 1$	$\times 1/2$	$\times 1/4$	$\times 1/8$	Avg.	$\times 1$	$\times 1/2$	$\times 1/4$	$\times 1/8$	Avg.
TensoRF	33.22	33.27	30.23	26.77	30.87	0.964	0.972	0.968	0.953	0.964	0.047	0.034	0.049	0.079	0.052
3DGS	33.57	27.04	21.43	17.74	24.95	0.970	0.950	0.876	0.767	0.891	0.037	0.036	0.071	0.130	0.068
Scaffold-GS	31.76	27.46	22.14	18.34	24.92	0.961	0.949	0.886	0.784	0.895	0.050	0.041	0.067	0.121	0.070
2DGs	31.81	26.73	20.21	16.41	23.79	0.965	0.946	0.846	0.711	0.867	0.048	0.052	0.102	0.177	0.095
3D-HGS	33.70	27.34	21.71	17.99	25.19	0.970	0.953	0.883	0.777	0.896	0.037	0.035	0.067	0.124	0.066
Tri-MipRF	32.86	32.80	28.44	24.22	29.58	0.959	0.968	0.955	0.924	0.951	0.056	0.039	0.051	0.075	0.055
3DGS+EWA	33.60	32.05	28.28	25.11	29.76	0.970	0.972	0.963	0.946	0.962	0.039	0.027	0.033	0.045	0.036
3DGS+SS	33.86	31.47	26.53	22.41	28.57	0.971	0.972	0.952	0.906	0.950	0.036	0.024	0.035	0.064	0.040
Mip-Splatting	33.54	34.09	31.50	27.80	31.73	0.969	0.976	0.977	0.968	0.973	0.038	0.022	0.022	0.032	0.028
Analytic-Splatting	33.78	34.20	31.16	27.22	31.59	0.970	0.977	0.977	0.965	0.972	0.036	0.022	0.025	0.037	0.030
Scaffold-GS+GB	30.22	32.02	33.84	33.80	32.47	0.949	0.964	0.976	0.983	0.968	0.070	0.041	0.025	0.019	0.039
2DGs+GB	31.96	33.53	34.93	34.74	33.79	0.960	0.970	0.979	0.985	0.974	0.055	0.033	0.022	0.015	0.031
Mip-Splatting+GB _{test}	33.45	35.37	36.98	36.36	35.54	0.969	0.978	0.984	0.988	0.980	0.038	0.021	0.014	0.012	0.021
Analytic-Splatting+GB _{test}	33.62	35.72	37.36	36.51	35.80	0.970	0.979	0.985	0.989	0.981	0.037	0.020	0.013	0.011	0.020
Gaussian Blending	33.92 35.80 36.82 35.79 35.58					0.970	0.979	0.985	0.988	0.981	0.036	0.020	0.013	0.012	0.020

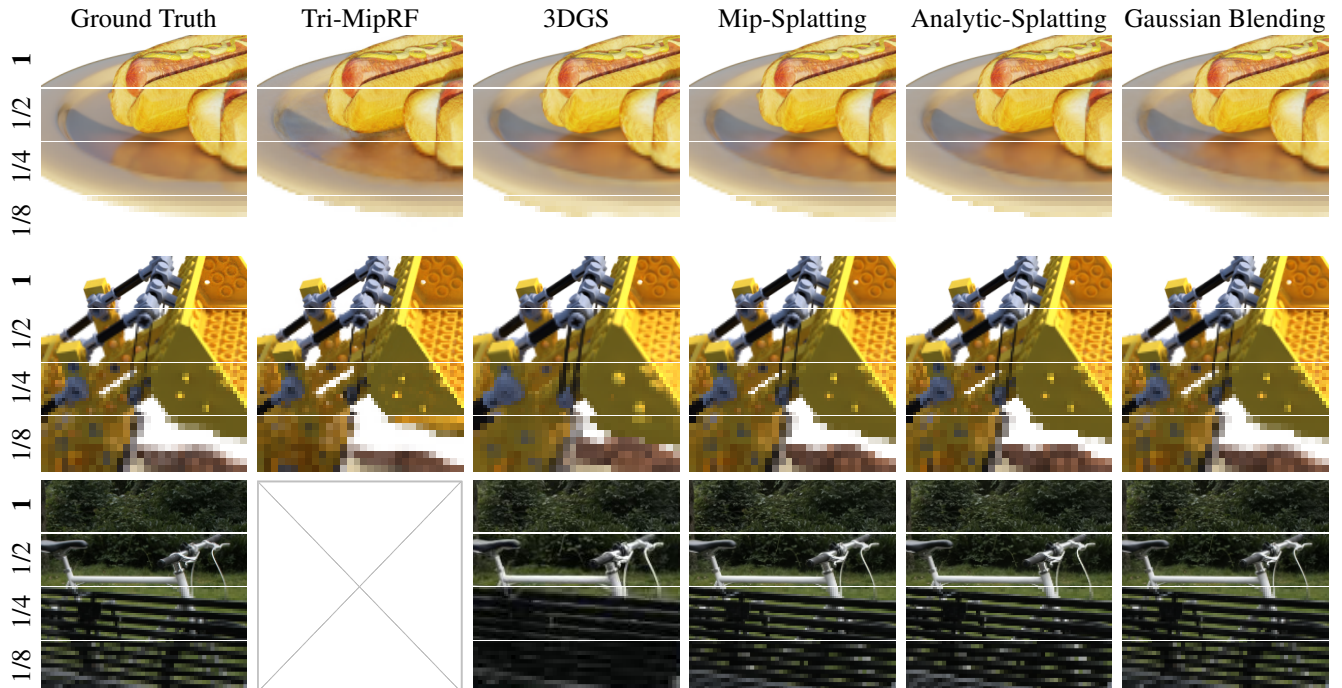


Figure 4: Qualitative results of zoom-out setting (Single-scale training ($\times 1$ resolution) and multi-scale testing). The training resolution is highlighted in **bold**. Our Gaussian Blending effectively suppresses pixel-level dilation in zoom-out scenarios (e.g., the disk edge in the top scene at $\times 1/8$ resolution).

Figure 2(c). This dynamic update allows us to handle spatial occlusions by adaptively shrinking the rendering window in regions of lower transmittance, reducing the influence of overlapping splats. Consequently, each splat is blended according to its spatial distribution, effectively and efficiently reducing intra-pixel aliasing within a single rendering pass.

Finally, we compute the final pixel color as

$$C_p = \sum_{i=1}^N c_i \int w_i(x) dx. \quad (12)$$

4 Experiments

4.1 Experiment Setup

Datasets. We evaluate novel view synthesis performance on two standard datasets: multi-scale Blender (Mildenhall et al. 2021; Barron et al. 2021) and multi-scale Mip-NeRF 360 dataset (Barron et al. 2022). The Blender dataset comprises eight synthetic scenes, each containing 100 training and 200 test images, with a resolution of 800×800 pixels. The Mip-NeRF 360 dataset includes nine real-world scenes (five out-

Table 2: Single-scale training ($\times 1/8$ resolution) and multi-scale testing results on the multi-scale Blender dataset. The best results are highlighted in **bold**.

	PSNR \uparrow					SSIM \uparrow					LPIPS \downarrow				
	$\times 1$	$\times 1/2$	$\times 1/4$	$\times 1/8$	Avg.	$\times 1$	$\times 1/2$	$\times 1/4$	$\times 1/8$	Avg.	$\times 1$	$\times 1/2$	$\times 1/4$	$\times 1/8$	Avg.
TensoRF	25.42	26.57	29.02	32.87	28.47	0.874	0.902	0.946	0.977	0.925	0.159	0.132	0.078	0.028	0.099
3DGS	18.51	19.90	23.33	34.72	24.11	0.824	0.832	0.905	0.984	0.886	0.163	0.136	0.072	0.016	0.097
Scaffold-GS	16.37	17.71	21.35	34.06	22.37	0.802	0.797	0.867	0.980	0.862	0.187	0.172	0.106	0.020	0.121
2DGS	22.87	23.59	25.46	31.85	25.94	0.864	0.879	0.920	0.973	0.909	0.159	0.139	0.087	0.031	0.104
3D-HGS	18.87	20.16	23.39	35.08	24.38	0.826	0.834	0.904	0.984	0.887	0.169	0.142	0.073	0.015	0.100
Tri-MipRF	21.99	22.91	25.84	33.93	26.17	0.809	0.821	0.888	0.979	0.874	0.240	0.232	0.170	0.023	0.166
3DGS+EWA	21.76	23.15	26.64	34.32	26.47	0.834	0.871	0.938	0.983	0.907	0.231	0.184	0.095	0.019	0.132
3DGS+SS	20.98	22.47	26.33	36.96	26.68	0.851	0.877	0.942	0.987	0.914	0.136	0.100	0.048	0.012	0.074
Mip-Splatting	25.97	27.24	30.06	35.29	29.64	0.892	0.920	0.959	0.985	0.939	0.150	0.117	0.056	0.015	0.084
Analytic-Splatting	25.45	26.98	30.04	35.63	29.53	0.878	0.914	0.956	0.984	0.933	0.138	0.102	0.051	0.015	0.077
Scaffold-GS+GB	26.57	28.02	31.11	35.92	30.41	0.886	0.918	0.958	0.985	0.937	0.149	0.116	0.061	0.016	0.085
2DGS+GB	25.49	26.94	29.47	33.05	28.74	0.880	0.908	0.947	0.976	0.928	0.151	0.120	0.067	0.025	0.091
Mip-Splatting+GB _{test}	25.95	27.17	29.67	33.69	29.12	0.891	0.919	0.958	0.984	0.938	0.151	0.120	0.059	0.016	0.087
Analytic-Splatting+GB _{test}	25.37	26.87	29.51	33.34	28.78	0.876	0.912	0.954	0.982	0.931	0.139	0.104	0.053	0.017	0.078
Gaussian Blending	26.74	28.53	31.97	36.92	31.04	0.891	0.927	0.965	0.987	0.943	0.132	0.092	0.042	0.012	0.069

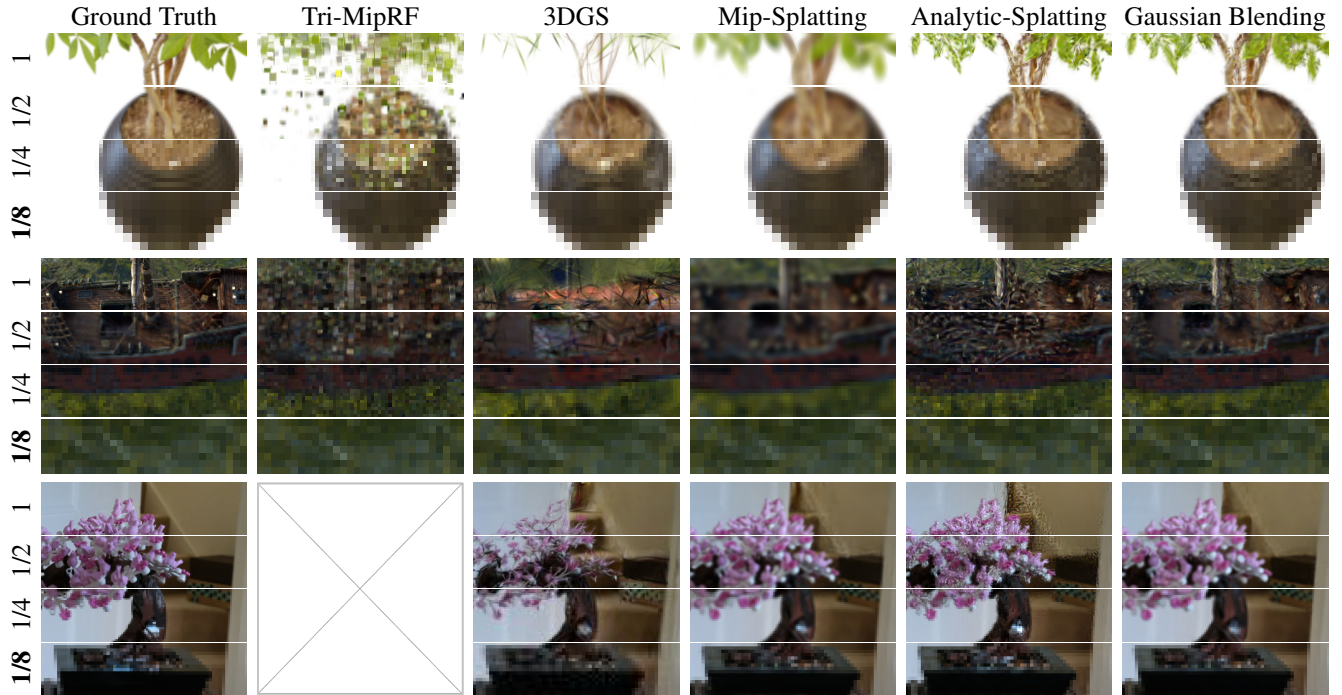


Figure 5: Qualitative results of zoom-in setting (Single-scale training ($\times 1/8$ resolution) and multi-scale testing). The training resolution is highlighted in **bold**. Our Gaussian Blending effectively prevents erosion in zoom-in scenarios (e.g., the leaves in the top scene at $\times 1$ resolution).

door and four indoor scenes). Following standard practice, we use every eighth image for testing, and the other images for training. For both datasets, to assess rendering quality at varying sampling rates, we also include downsampled versions of each image by factors of 2, 4, and 8.

Performance Measures. We report results using three standard metrics: Peak Signal-to-Noise Ratio (PSNR), Structural Similarity Index Measure (SSIM), and Learned Perceptual Image Patch Similarity (LPIPS).

Implementation. Our Gaussian Blending algorithm is

implemented in CUDA. Through careful optimization, it achieves identical time complexity and comparable runtime performance to 3DGS models without additional memory overhead. Following prior works, we train all models for 30k iterations using identical hyperparameters across all scenes.

Baselines. We compare the performance against state-of-the-art real-time NVS and anti-aliased NVS methods, including (i) five standard NVS approaches: TensoRF (Chen et al. 2022), 3DGS (Kerbl et al. 2023), Scaffold-GS (Lu et al. 2024), 2DGS (Huang et al. 2024), and 3D-HGS (Li

Table 3: PSNR scores for multi-scale testing on the multi-scale Mip-NeRF 360 dataset. The best results are highlighted in **bold**.

	(a) Single-scale Training ($\times 1$ res)					(b) Single-scale Training ($\times 1/8$ res)					(c) Multi-scale Training				
	$\times 1$	$\times 1/2$	$\times 1/4$	$\times 1/8$	Avg.	$\times 1$	$\times 1/2$	$\times 1/4$	$\times 1/8$	Avg.	$\times 1$	$\times 1/2$	$\times 1/4$	$\times 1/8$	Avg.
3DGS	27.63	25.76	21.98	19.34	23.68	17.25	18.73	22.41	30.60	22.25	26.85	27.89	28.28	27.17	27.55
Scaffold-GS	27.27	26.05	22.48	19.70	23.87	17.09	18.43	21.98	31.06	22.14	26.61	27.75	28.42	27.23	27.50
2DGS	26.71	25.99	21.84	18.41	23.24	20.92	21.66	23.85	29.49	23.98	25.70	26.73	27.72	26.52	26.67
3D-HGS	28.07	26.12	22.13	19.36	23.92	18.16	19.59	23.10	31.26	23.03	27.47	28.62	29.40	28.75	28.56
3DGS+EWA	27.67	28.40	28.23	27.19	27.87	20.27	21.76	24.90	29.38	24.08	26.50	27.75	28.93	29.25	28.11
3DGS+SS	27.67	27.71	25.47	22.59	25.86	20.14	21.50	24.84	31.22	24.42	27.37	28.54	29.69	29.44	28.76
Mip-Splatting	27.50	28.27	29.22	28.89	28.47	24.35	25.51	27.79	30.95	27.15	27.41	28.46	30.01	31.13	29.25
Analytic-Splatting	27.36	28.12	28.92	28.51	28.23	23.00	24.37	27.12	30.86	26.34	27.31	28.40	29.98	31.17	29.21
Gaussian Blending	27.55	28.62	29.92	30.58	29.17	24.86	25.97	28.13	30.90	27.47	27.58	28.77	30.24	31.54	29.53

et al. 2025), (ii) one mipmap-based anti-aliasing method: Tri-MipRF (Hu et al. 2023), and (iii) three prefiltering-based anti-aliasing methods: 3DGS+EWA (Zwicker et al. 2001), Mip-Splatting (Yu et al. 2024b), and Analytic-Splatting (Liang et al. 2024b). We also include a supersampling baseline, 3DGS+SS, which renders images at the $2 \times$ target resolution and then downsamples it by half. Note that TensoRF and Tri-MipRF are tested only in the Blender dataset, since they are not applicable to unbounded scenes.

Gaussian Blending is a general rendering formulation that can function both as a standalone model and as a drop-in renderer for existing NVS frameworks. We demonstrate its flexibility across three representative integration settings: (i) for anti-aliased NVS methods such as Mip-Splatting and Analytic-Splatting, we retain each model’s original training pipeline and simply substitute their rendering module with our kernel at test time, denoted as *Mip-Splatting+GB_{test}* and *Analytic-Splatting+GB_{test}*; (ii) for general 3DGS-based frameworks such as Scaffold-GS, we replace the original CUDA kernel with our Gaussian Blending kernel during both training and inference, denoted as *Scaffold-GS+GB*; and (iii) for models using non-3DGS rendering backbones, such as 2DGS, we reimplement our spatial alpha blending concept within their native kernel, yielding *2DGS+GB*.

4.2 Approximation Error Analysis

As shown in Figure 3, scalar alpha blending methods—such as 3DGS, 3DGS+SS, Mip-Splatting, and Analytic-Splatting—exhibit noticeable transmittance errors. In particular, their transmittance error ΔT become negative, indicating dilation, where the occluded splat contributes excessively to the pixel color. Although Analytic-Splatting analytically integrates each splat’s response over the pixel area, it still relies on scalar alpha blending when compositing multiple splats. As a result, the first splat’s contribution is computed accurately, but the second splat, which spatially overlaps with the first splat, is blended using an averaged transmittance value. This averaging neglects spatial occlusion, causing the second splat to receive an erroneously higher weight and leading to over-attenuated (dilated) transmittance after rendering. In contrast, our Gaussian Blending dynamically adjusts the transmittance window to explicitly account for spatial occlusion. As a result, Gaussian Blending achieves on average more than $5 \times$ lower transmittance

Table 4: Multi-scale training and multi-scale testing results on the multi-scale Blender dataset.

	PSNR \uparrow				
	$\times 1$	$\times 1/2$	$\times 1/4$	$\times 1/8$	Avg.
TensoRF	33.03	33.92	30.99	27.26	31.30
3DGS	30.19	31.38	30.59	27.05	29.90
Scaffold-GS	28.56	29.85	29.41	26.08	28.48
2DGS	27.95	29.39	30.31	26.23	28.47
3D-HGS	30.96	32.40	31.90	28.70	30.99
Tri-MipRF	32.60	34.18	34.97	35.32	34.27
3DGS+EWA	30.34	31.78	32.45	31.50	31.52
3DGS+SS	32.12	33.81	33.98	31.13	32.76
Mip-Splatting	32.93	34.68	35.79	35.48	34.72
Analytic-Splatting	33.28	35.02	36.07	35.90	35.07
Scaffold-GS+GB	29.68	31.56	33.81	34.87	32.48
2DGS+GB	31.12	32.89	34.99	36.26	33.81
Mip-Splatting+GB _{test}	32.85	34.69	36.32	37.00	35.22
Analytic-Splatting+GB _{test}	33.15	35.09	36.52	36.44	35.30
Gaussian Blending	33.50	35.48	37.38	38.39	36.19

error compared to previous methods.

4.3 Single-Scale Training and Multi-Scale Testing

To evaluate anti-aliasing performance at sampling rates not encountered during training, we experiment with a single-scale training and multi-scale testing setup. Specifically, models are trained at each of the resolutions ($\times 1$, $\times 1/2$, $\times 1/4$, or $\times 1/8$), and their rendering quality is tested across all resolutions. Quantitative results demonstrate that Gaussian Blending consistently outperforms competing methods in both zoom-out (Table 7 and 3(a)) and zoom-in (Table 10 and 3(b)) scenarios, achieving particularly impressive gains in zoom-out settings. Moreover, our qualitative results in Figure 15 and 16 further illustrate that Gaussian Blending successfully mitigates aliasing artifacts at sampling rates unseen during training.

Models employing scalar alpha blending suffer from pixel-level dilation and erosion artifacts. Mipmap-based models struggle with rendering at unseen sampling rates due to extrapolation issues, thus creating floaters from the unseen resolution mipmap. Mip-Splatting avoids sparsity issues during zoom-in due to its 3D smoothing filter, but it produces blurry renderings and fails to accurately reconstruct high-frequency details. In contrast, our model prevents saturation of the transmittance by avoiding rendering

Table 5: Efficiency comparison across different NVS methods. We report average zoom-out quality (PSNR), $\times 1$ resolution rendering speed (FPS), training time, and storage memory usage in the multi-scale Blender dataset.

Method	PSNR \uparrow	FPS \uparrow	Training Time \downarrow	Memory (MB) \downarrow
TensoRF	30.87	0.83	18m 18s	72.59
3DGS	24.95	131.80	16m 2s	61.86
Scaffold-GS	24.92	134.68	12m 2s	8.14
2DGS	23.79	95.35	19m 12s	25.97
3D-HGS	25.19	184.33	10m 43s	61.52
Tri-MipRF	29.58	3.18	6m 33s	58.31
3DGS+EWA	29.76	104.71	13m 18s	56.19
3DGS+SS	28.57	79.21	21m 56s	60.84
Mip-Splatting	31.73	131.58	10m 10s	71.28
Analytic-Splatting	31.59	72.07	11m 37s	69.62
Gaussian Blending-7K	34.02	128.49	2m 3s	55.17
Gaussian Blending-15K	35.24	112.45	6m 6s	72.82
Gaussian Blending-30K	35.58	123.08	12m 34s	72.82

in a low transmittance area. As shown in Table 5, Gaussian Blending achieves real-time rendering without any additional memory overhead and converges within only 7K iterations—over 3 \times faster than the baselines—while already surpassing them in anti-aliasing performance.

4.4 Multi-Scale Training and Multi-Scale Testing

To further demonstrate the robustness of Gaussian Blending in handling varying sampling rates, we also experiment with multi-scale training and multi-scale testing. In this scenario, models are simultaneously trained on images across all four resolutions: $\times 1$, $\times 1/2$, $\times 1/4$, and $\times 1/8$, and then evaluated on the same scales to assess whether models can effectively learn from multi-scale data.

Table 11 and Table 3(c) show that our model outperforms all other real-time and unbounded NVS methods. Our model consistently captures spatial variations without introducing dilation artifacts across diverse sampling rates, even when trained on complex scenes spanning a wide range of sampling rates.

4.5 Drop-in Gaussian Blending

To further demonstrate the generality of our formulation, we apply Gaussian Blending to various NVS frameworks with different rendering backbones, following the three integration types described in Section 4.1. Across all integration settings, Gaussian Blending consistently enhances rendering quality and anti-aliasing performance. Remarkably, even when the splat size and spatial distribution are learned according to each model’s native renderer—such as in Mip-Splatting and Analytic-Splatting—simply replacing their rendering kernel with ours *at test time only* prevents pixel-level dilation. This demonstrates that Gaussian Blending offers a more physically consistent integration of alpha and transmittance, effectively reducing pixel-level dilation and preserving high-frequency details, all without retraining or modifying the underlying representation.

Moreover, Gaussian Blending exhibits strong robustness to unseen sampling rates, including both zoom-in and zoom-out scenarios. While conventional scalar alpha blending tends to blur boundaries under high sampling rates and in-

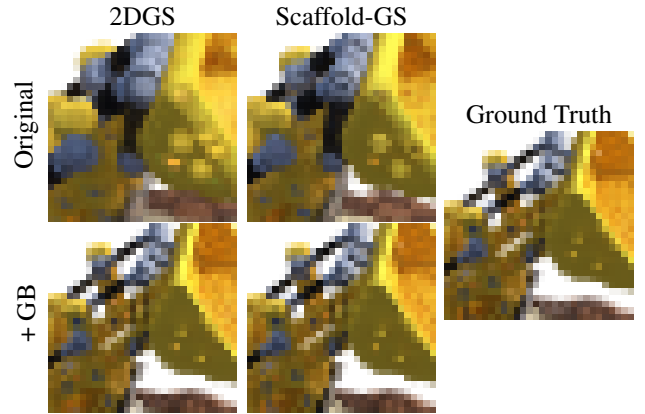


Figure 6: Qualitative comparison of Gaussian Blending applied to 2DGS and Scaffold-GS.

introduce staircase-like dilation under low rates, our method maintains stable transmittance accumulation and consistent image quality across scales. When the model is trained directly using our kernel, the improvements become even more pronounced across all resolutions, confirming that Gaussian Blending functions as a unified rendering formulation suitable for both training and inference. Qualitative comparisons in Figure 6 further support these findings: both *Scaffold-GS+GB* and *2DGS+GB* deliver sharper object boundaries compared to their original rendering kernels. Our spatial alpha blending concept generalizes beyond 3DGS and can be applied to any neural rendering framework that employs an integrable alpha or density function.

5 Conclusion

We introduced *Gaussian Blending*, a novel spatial alpha blending method to address intra-pixel aliasing artifacts arising from traditional scalar alpha blending used in existing novel view synthesis (NVS) methods. By representing alpha and transmittance as spatially varying distributions within pixel regions, Gaussian Blending effectively mitigates erosion and dilation artifacts when rendering views at sampling rates unseen during training. Leveraging the spatial coherence of Gaussian splats, our approach maintains identical computational complexity and memory usage to standard 3DGS. Extensive experiments demonstrate that Gaussian Blending consistently synthesizes higher-quality views across both single-scale and multi-scale scenarios without additional priors or retraining. Furthermore, it can be seamlessly integrated as a drop-in replacement for existing NVS frameworks, providing an efficient and practical anti-aliasing solution.

While Gaussian Blending performs well even on complex real scenes, it cannot resolve boundary blurring caused by real camera effects such as diffraction, chromatic aberration, and defocus blur. Additionally, since the zoom-in setting is an ill-posed problem, high-frequency noise can occur when highly specular objects are present (e.g., the *drums* scene). Addressing these issues to further enhance performance in complex real-world scenarios remains future work.

Acknowledgments

This work was supported by Institute of Information & communications Technology Planning & Evaluation (IITP) grant funded by the Korea government (MSIT) (No. RS-2022-II220156, Fundamental research on continual meta-learning for quality enhancement of casual videos and their 3D metaverse transformation), Institute of Information & Communications Technology Planning & Evaluation(IITP) grant funded by the Korea government(MSIT) (RS-2025-25442338, AI star Fellowship Support Program(Seoul National Univ.)), Basic Science Research Program through the National Research Foundation of Korea(NRF) funded by the Ministry of Education(RS-2023-00274280), IITP(Institute of Information & Communications Technology Planning & Evaluation)-ITRC(Information Technology Research Center) grant funded by the Korea government(Ministry of Science and ICT)(IITP-2025-RS-2024-00437633), and Center for Applied Research in Artificial Intelligence(CARAI) grant funded by Defense Acquisition Program Administration(DAPA) and Agency for Defense Development(ADD) (UD230017TD). Gunhee Kim is the corresponding author.

References

- Barron, J. T.; Mildenhall, B.; Tancik, M.; Hedman, P.; Martin-Brualla, R.; and Srinivasan, P. P. 2021. Mip-nerf: A multiscale representation for anti-aliasing neural radiance fields. In *Proceedings of the IEEE/CVF international conference on computer vision*, 5855–5864.
- Barron, J. T.; Mildenhall, B.; Verbin, D.; Srinivasan, P. P.; and Hedman, P. 2022. Mip-nerf 360: Unbounded anti-aliased neural radiance fields. In *Proceedings of the IEEE/CVF conference on computer vision and pattern recognition*, 5470–5479.
- Bulò, S. R.; Porzi, L.; and Kortschieder, P. 2024. Revising Densification in Gaussian Splatting. *arXiv:2404.06109*.
- Chen, A.; Xu, Z.; Geiger, A.; Yu, J.; and Su, H. 2022. Tensorf: Tensorial radiance fields. In *European conference on computer vision*, 333–350. Springer.
- Feng, X.; He, Y.; Wang, Y.; Yang, Y.; Li, W.; Chen, Y.; Kuang, Z.; Fan, J.; Jun, Y.; et al. 2024. SRGS: Super-Resolution 3D Gaussian Splatting. *arXiv preprint arXiv:2404.10318*.
- Haque, A.; Tancik, M.; Efros, A. A.; Holynski, A.; and Kanazawa, A. 2023. Instruct-nerf2nerf: Editing 3d scenes with instructions. In *Proceedings of the IEEE/CVF International Conference on Computer Vision*, 19740–19750.
- Hu, W.; Wang, Y.; Ma, L.; Yang, B.; Gao, L.; Liu, X.; and Ma, Y. 2023. Tri-miprf: Tri-mip representation for efficient anti-aliasing neural radiance fields. In *Proceedings of the IEEE/CVF International Conference on Computer Vision*, 19774–19783.
- Huang, B.; Yu, Z.; Chen, A.; Geiger, A.; and Gao, S. 2024. 2D Gaussian Splatting for Geometrically Accurate Radiance Fields. In *SIGGRAPH 2024 Conference Papers*. Association for Computing Machinery.
- Jeong, J.; Koo, J.; Zhang, Q.; and Kim, G. 2024. ESR-NeRF: Emissive Source Reconstruction Using LDR Multi-view Images. In *Proceedings of the IEEE/CVF Conference on Computer Vision and Pattern Recognition*, 4598–4609.
- Kerbl, B.; Kopanas, G.; Leimkühler, T.; and Drettakis, G. 2023. 3d gaussian splatting for real-time radiance field rendering. *ACM Trans. Graph.*, 42(4): 139–1.
- Li, H.; Liu, J.; Sznaier, M.; and Camps, O. 2025. 3D-HGS: 3D Half-Gaussian Splatting. In *Proceedings of the IEEE/CVF Conference on Computer Vision and Pattern Recognition (CVPR)*, 10996–11005.
- Li, J.; Shi, Y.; Cao, J.; Ni, B.; Zhang, W.; Zhang, K.; and Van Gool, L. 2024. Mipmap-GS: Let Gaussians Deform with Scale-specific Mipmap for Anti-aliasing Rendering. *CoRR*.
- Liang, Z.; Zhang, Q.; Feng, Y.; Shan, Y.; and Jia, K. 2024a. Gs-ir: 3d gaussian splatting for inverse rendering. In *Proceedings of the IEEE/CVF Conference on Computer Vision and Pattern Recognition*, 21644–21653.
- Liang, Z.; Zhang, Q.; Hu, W.; Zhu, L.; Feng, Y.; and Jia, K. 2024b. Analytic-splatting: Anti-aliased 3d gaussian splatting via analytic integration. In *European conference on computer vision*, 281–297. Springer.
- Lin, C.; Pan, P.; Yang, B.; Li, Z.; and Mu, Y. 2025. DiffSplat: Repurposing Image Diffusion Models for Scalable Gaussian Splat Generation. *arXiv preprint arXiv:2501.16764*.
- Lu, T.; Yu, M.; Xu, L.; Xiangli, Y.; Wang, L.; Lin, D.; and Dai, B. 2024. Scaffold-gs: Structured 3d gaussians for view-adaptive rendering. In *Proceedings of the IEEE/CVF Conference on Computer Vision and Pattern Recognition*, 20654–20664.
- Mildenhall, B.; Srinivasan, P. P.; Tancik, M.; Barron, J. T.; Ramamoorthi, R.; and Ng, R. 2021. Nerf: Representing scenes as neural radiance fields for view synthesis. *Communications of the ACM*, 65(1): 99–106.
- Moenne-Loccoz, N.; Mirzaei, A.; Perel, O.; de Lutio, R.; Martinez Esturo, J.; State, G.; Fidler, S.; Sharp, N.; and Gojcic, Z. 2024. 3D Gaussian Ray Tracing: Fast Tracing of Particle Scenes. *ACM Transactions on Graphics (TOG)*, 43(6): 1–19.
- Müller, T.; Evans, A.; Schied, C.; and Keller, A. 2022. Instant neural graphics primitives with a multiresolution hash encoding. *ACM transactions on graphics (TOG)*, 41(4): 1–15.
- Park, K.; Sinha, U.; Hedman, P.; Barron, J. T.; Bouaziz, S.; Goldman, D. B.; Martin-Brualla, R.; and Seitz, S. M. 2021. HyperNeRF: a higher-dimensional representation for topologically varying neural radiance fields. *ACM Transactions on Graphics (TOG)*, 40(6): 1–12.
- Poole, B.; Jain, A.; Barron, J. T.; and Mildenhall, B. 2023. DreamFusion: Text-to-3D using 2D Diffusion. In *The Eleventh International Conference on Learning Representations*.
- Pumarola, A.; Corona, E.; Pons-Moll, G.; and Moreno-Noguer, F. 2021. D-nerf: Neural radiance fields for dynamic scenes. In *Proceedings of the IEEE/CVF conference on computer vision and pattern recognition*, 10318–10327.

- Ren, K.; Jiang, L.; Lu, T.; Yu, M.; Xu, L.; Ni, Z.; and Dai, B. 2024. Octree-gs: Towards consistent real-time rendering with lod-structured 3d gaussians. *arXiv preprint arXiv:2403.17898*.
- Shannon, C. E. 1949. Communication in the presence of noise. *Proceedings of the IRE*, 37(1): 10–21.
- Sun, C.; Sun, M.; and Chen, H.-T. 2022. Direct voxel grid optimization: Super-fast convergence for radiance fields reconstruction. In *Proceedings of the IEEE/CVF conference on computer vision and pattern recognition*, 5459–5469.
- Wang, C.; Wu, X.; Guo, Y.-C.; Zhang, S.-H.; Tai, Y.-W.; and Hu, S.-M. 2022. Nerf-sr: High quality neural radiance fields using supersampling. In *Proceedings of the 30th ACM International Conference on Multimedia*, 6445–6454.
- Wang, P.; Liu, L.; Liu, Y.; Theobalt, C.; Komura, T.; and Wang, W. 2021. NeuS: Learning Neural Implicit Surfaces by Volume Rendering for Multi-view Reconstruction. *Advances in Neural Information Processing Systems*, 34: 27171–27183.
- Wu, T.; Wang, J.; Pan, X.; Xudong, X.; Theobalt, C.; Liu, Z.; and Lin, D. 2023. Voxurf: Voxel-based Efficient and Accurate Neural Surface Reconstruction. In *The Eleventh International Conference on Learning Representations*.
- Xia, J.; and Liu, L. 2025. Close-up-GS: Enhancing Close-Up View Synthesis in 3D Gaussian Splatting with Progressive Self-Training. *arXiv preprint arXiv:2503.09396*.
- Yan, Z.; Low, W. F.; Chen, Y.; and Lee, G. H. 2024. Multi-scale 3d gaussian splatting for anti-aliased rendering. In *Proceedings of the IEEE/CVF Conference on Computer Vision and Pattern Recognition*, 20923–20931.
- Yang, Z.; Yang, H.; Pan, Z.; and Zhang, L. 2024. Real-time Photorealistic Dynamic Scene Representation and Rendering with 4D Gaussian Splatting. In *The Twelfth International Conference on Learning Representations*.
- Yu, X.; Zhu, H.; He, T.; and Chen, Z. 2024a. GaussianSR: 3D Gaussian Super-Resolution with 2D Diffusion Priors. *CoRR*.
- Yu, Z.; Chen, A.; Huang, B.; Sattler, T.; and Geiger, A. 2024b. Mip-splatting: Alias-free 3d gaussian splatting. In *Proceedings of the IEEE/CVF conference on computer vision and pattern recognition*, 19447–19456.
- Zwicker, M.; Pfister, H.; Van Baar, J.; and Gross, M. 2001. EWA volume splatting. In *Proceedings Visualization, 2001. VIS'01.*, 29–538. IEEE.

A Approach

A.1 Forward Derivation

In this section, we provide a full derivation for computing the integral $\int w_i(x)dx$ and T_{i+1} in the spatial alpha blending process. To simplify integration over the 2D Gaussian, we align our coordinate system with the axes of each splat's window, similar to Analytic-Splatting (Liang et al. 2024b). In this coordinate system, we can separate and independently evaluate the integral $\int w_i(x)dx$ along each axis.

We first define the zeroth-, first- and second-order moments of the 1D Gaussian ($I_\sigma^0(a, b)$, $I_\sigma^1(a, b)$, $I_\sigma^2(a, b)$) as

$$\begin{aligned} I_\sigma^0(a, b) &= \int_a^b \exp\left(-\frac{x^2}{2\sigma^2}\right) dx \\ &= \sqrt{\frac{\pi}{2}}\sigma \left[\operatorname{erf}\left(\frac{b}{\sqrt{2}\sigma}\right) - \operatorname{erf}\left(\frac{a}{\sqrt{2}\sigma}\right) \right], \\ I_\sigma^1(a, b) &= \int_a^b x \exp\left(-\frac{x^2}{2\sigma^2}\right) dx \\ &= \sigma^2 \left(\exp\left(-\frac{a^2}{2\sigma^2}\right) - \exp\left(-\frac{b^2}{2\sigma^2}\right) \right), \\ I_\sigma^2(a, b) &= \int_a^b x^2 \exp\left(-\frac{x^2}{2\sigma^2}\right) dx \\ &= \sigma^2 \left(I_\sigma^0(a, b) + a \exp\left(-\frac{a^2}{2\sigma^2}\right) - b \exp\left(-\frac{b^2}{2\sigma^2}\right) \right). \end{aligned} \quad (13)$$

Using the zeroth-order moment of the 1D Gaussian $I_\sigma^0(a, b)$, we express the integrated weight as

$$\begin{aligned} \int w_i(x)dx &= \int_{u_1}^{u_2} \int_{v_1}^{v_2} t_i o_i \exp\left(-\frac{x^2}{2\sigma_1^2} - \frac{y^2}{2\sigma_2^2}\right) dx dy \\ &= t_i o_i \int_{u_1}^{u_2} \exp\left(-\frac{x^2}{2\sigma_1^2}\right) dx \int_{v_1}^{v_2} \exp\left(-\frac{y^2}{2\sigma_2^2}\right) dy \\ &= t_i o_i I_{\sigma_1}^0(u_1, u_2) I_{\sigma_2}^0(v_1, v_2). \end{aligned} \quad (14)$$

Next, we can use the integrated weight to compute the zeroth-order moment of $T_i(x)(1 - \alpha_i(x))$ as

$$\begin{aligned} M_i^0 &= \int_{u_1}^{u_2} \int_{v_1}^{v_2} t_i (1 - o_i) \exp\left(-\frac{x^2}{2\sigma_1^2} - \frac{y^2}{2\sigma_2^2}\right) dx dy \\ &= t_i l_{i,1} l_{i,2} - \int_{u_1}^{u_2} \int_{v_1}^{v_2} t_i o_i \exp\left(-\frac{x^2}{2\sigma_1^2} - \frac{y^2}{2\sigma_2^2}\right) dx dy \\ &= t_i l_{i,1} l_{i,2} - \int w_i(x)dx \\ &= t_i l_{i,1} l_{i,2} - t_i o_i I_{\sigma_1}^0(u_1, u_2) I_{\sigma_2}^0(v_1, v_2). \end{aligned} \quad (15)$$

The zeroth-order moment M_i^0 means the accumulated transmittance value after rendering the i -th splat, which plays a similar role to the transmittance value T_i^s in the scalar alpha blending. This simplification proves that our method always maintains $\int T_{i+1}(x)dx = \int T_i(x) - w_i(x)dx$, which is crucial for the physical correctness of the rendering process.

We can also simplify the first-, and second-order moments (M_i^1, M_i^2) of $T_i(x)(1 - \alpha_i(x))$ as

$$\begin{aligned} M_i^1 &= \int_{u_1}^{u_2} \int_{v_1}^{v_2} t_i (1 - o_i) \exp\left(-\frac{x^2}{2\sigma_1^2} - \frac{y^2}{2\sigma_2^2}\right) \begin{bmatrix} x \\ y \end{bmatrix} dx dy \\ &= t_i l_{i,1} l_{i,2} \begin{bmatrix} u \\ v \end{bmatrix} \\ &\quad - t_i o_i \begin{bmatrix} \int_{u_1}^{u_2} x \exp\left(-\frac{x^2}{2\sigma_1^2}\right) dx \int_{v_1}^{v_2} \exp\left(-\frac{y^2}{2\sigma_2^2}\right) dy \\ \int_{u_1}^{u_2} \exp\left(-\frac{x^2}{2\sigma_1^2}\right) dx \int_{v_1}^{v_2} y \exp\left(-\frac{y^2}{2\sigma_2^2}\right) dy \end{bmatrix} \\ &= t_i l_{i,1} l_{i,2} \begin{bmatrix} u \\ v \end{bmatrix} - t_i o_i \begin{bmatrix} I_{\sigma_1}^1(u_1, u_2) \cdot I_{\sigma_2}^0(v_1, v_2) \\ I_{\sigma_1}^0(u_1, u_2) \cdot I_{\sigma_2}^1(v_1, v_2) \end{bmatrix}, \end{aligned} \quad (16)$$

$$\begin{aligned} M_i^2 &= \int_{u_1}^{u_2} \int_{v_1}^{v_2} t_i (1 - o_i) \exp\left(-\frac{x^2}{2\sigma_1^2} - \frac{y^2}{2\sigma_2^2}\right) \begin{bmatrix} x^2 \\ y^2 \end{bmatrix} dx dy \\ &= t_i l_{i,1} l_{i,2} \left(\begin{bmatrix} u^2 \\ v^2 \end{bmatrix} + \frac{1}{12} l_i^2 \right) \\ &\quad - t_i o_i \left[\begin{bmatrix} \int_{u_1}^{u_2} x^2 \exp\left(-\frac{x^2}{2\sigma_1^2}\right) dx \int_{v_1}^{v_2} \exp\left(-\frac{y^2}{2\sigma_2^2}\right) dy \\ \int_{u_1}^{u_2} \exp\left(-\frac{x^2}{2\sigma_1^2}\right) dx \int_{v_1}^{v_2} y^2 \exp\left(-\frac{y^2}{2\sigma_2^2}\right) dy \end{bmatrix} \right] \\ &= t_i l_{i,1} l_{i,2} \left(\begin{bmatrix} u^2 \\ v^2 \end{bmatrix} + \frac{1}{12} l_i^2 \right) \\ &\quad - t_i o_i \begin{bmatrix} I_{\sigma_1}^2(u_1, u_2) \cdot I_{\sigma_2}^0(v_1, v_2) \\ I_{\sigma_1}^0(u_1, u_2) \cdot I_{\sigma_2}^2(v_1, v_2) \end{bmatrix}. \end{aligned} \quad (17)$$

Then, the mean of $T_i(x)(1 - \alpha_i(x))$ in the α_i -aligned coordinate system can be calculated as $\frac{M_i^1}{M_i^0}$, the variance as $\frac{M_i^2}{M_i^0} - \left(\frac{M_i^1}{M_i^0}\right)^2$, and the accumulated transmittance value as M_i^0 . Leveraging the properties of a 2D uniform distribution, we derive the 2D screen-space expression for T_{i+1} as

$$x_{i+1} = \mu'_i + [e_1, e_2] \frac{M_i^1}{M_i^0}, \quad (18a)$$

$$l_{i+1} = \sqrt{12 \left(\frac{M_i^2}{M_i^0} - \left(\frac{M_i^1}{M_i^0} \right)^2 \right)}, \quad (18b)$$

$$t_{i+1} = \frac{M_i^0}{l_{i+1,1} l_{i+1,2}}. \quad (18c)$$

Note that x_{i+1} is rotated back to the original coordinate system using the inverse rotation matrix $[e_1, e_2]$. This explicitly preserves the total transmittance mass, mean, and variance in terms of t_i , x_i , and l_i , ensuring a physically accurate rendering process.

A.2 Forward Visualization

To provide deeper understanding of the difference between scalar alpha blending and our Gaussian Blending, we visualize the rendering process in Figure 7. Scalar alpha blending first computes the scalar alpha value of each splat independently, and then blends the splats using this scalar alpha and

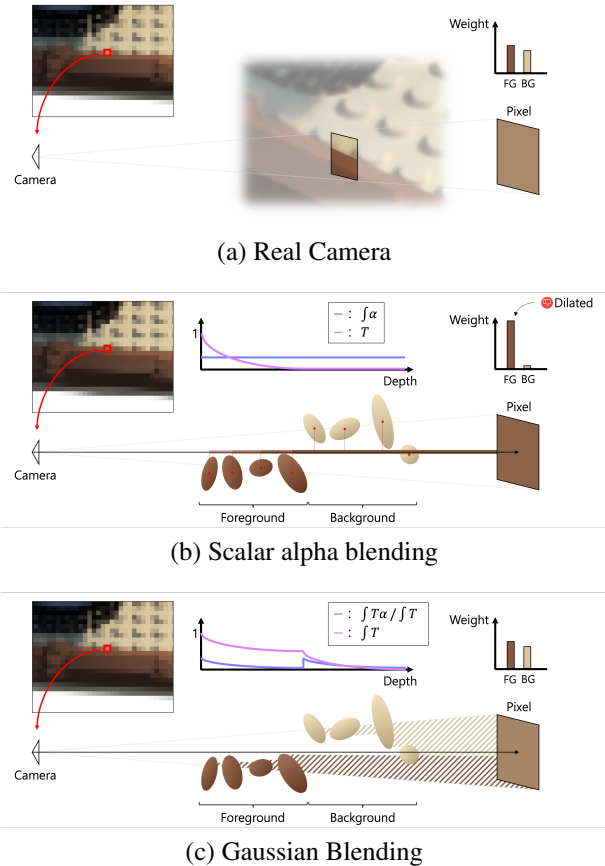


Figure 7: Comparison of rendering foreground splats and background splats using (a) a real camera, (b) scalar alpha blending, and (c) our Gaussian Blending.

scalar transmittance evaluated at the pixel center, which removes the spatial information of the splats. As a result, splats with similar 2D Gaussian projections yield identical alpha values (denoted as $\int \alpha$ in Figure 7(b)), regardless of their spatial occlusions. This approach causes undesired dilation of splats, rapidly saturating the transmittance value (denoted as T), and thus making background splats invisible in the final rendering.

In contrast, our Gaussian Blending considers alpha and transmittance as spatially varying distributions rather than scalar values. During the rendering process, the transmittance is spatially consumed where each splat is located. Consequently, overlapping splats have significantly lower average alpha values (denoted as $\int T \alpha / \int T$ in Figure 7(c)), ensuring that non-overlapping background splats remain clearly visible in the final rendering.

We also illustrate several examples of the transition from T_i to T_{i+1} in Figure 8. First, when a very large splat overlaps entirely with T_i , the splat does not affect the window range of the transmittance but lowers the overall transmittance value t_i . Second, when a splat partially overlaps with T_i from the side, the transmittance is reduced in the overlapped region, causing T_{i+1} to narrow toward the non-overlapping

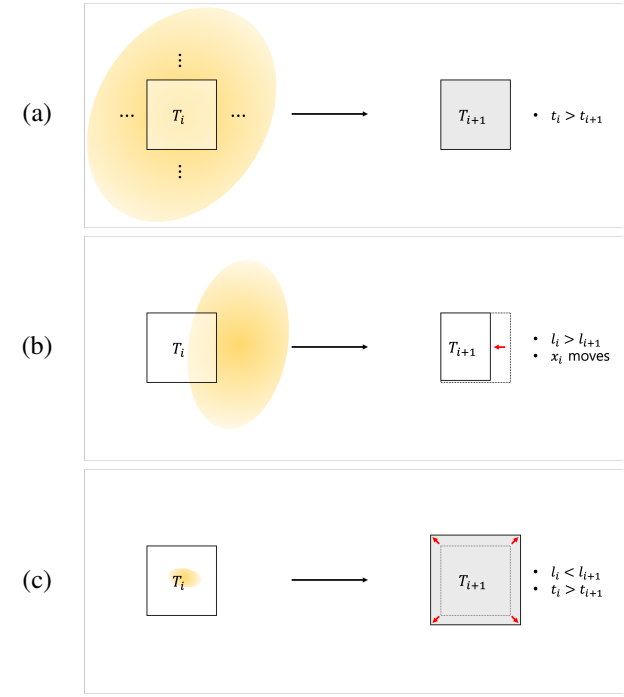


Figure 8: Example of transmittance calculation for three different cases.

region. Moreover, despite using a 2D uniform distribution, our method can also handle cases where small splats create holes in the transmittance. Specifically, when a very small splat intersects with T_i , the outer region without the splat dominates the transmittance, thus enlarging the window of T_{i+1} and reducing the influence of the region occupied by the splat in subsequent rendering steps.

B Implementation Details

B.1 Numerical Stability and Optimization

Analytic-Splatting approximates the Gaussian integral using a sigmoid-like function, as the integral of the Gaussian distribution cannot be expressed in a closed form. In contrast, our method directly leverages the error function (erf), resulting in a simpler, more accurate, and numerically stable calculation of the Gaussian integral. Additionally, when the window range of T_i becomes extremely small or large relative to a splat, the calculation of T_{i+1} may become numerically unstable. Thus, when the range falls outside $[0.1\sigma, 10^6\sigma]$, we assume that the splat does not alter the window range of T_i and instead perform scalar alpha blending at the center of T_i .

Although our Gaussian Blending adjusts the window from T_i to T_{i+1} during the forward pass, accurately reconstructing T_i from T_{i+1} in the backward pass becomes significantly challenging. A fully accurate backward process requires intermediate T_i buffers and sequentially propagating gradients using the chain rule from back to front. This backward pass is both slow and memory-intensive, and also causes unstable training due to accumulated errors in the gradient com-

putation. To resolve this issue, we employ a stop-gradient operation on the window range calculation. With this stop-gradient, as in 3DGS, each splat can independently compute both direct and indirect influences on pixels, lowering the gradient error accumulation. Additionally, by calculating gradients from front to back, we can completely eliminate the intermediate buffers, making the backward pass equivalent to conventional 3DGS and its variants in terms of memory usage and time complexity. Empirically, full backward and stop-gradient-based backward have no noticeable performance degradation, except in speed and stability. As a result, our method achieves a comparable or even faster rendering speed to 3DGS and its variants, with approximately 123 FPS.

B.2 Datasets

We find that previous works, including 3DGS (Kerbl et al. 2023) and its variants such as Mip-Splatting (Yu et al. 2024b) and Analytic-Splatting (Liang et al. 2024b), compute LPIPS incorrectly due to improper normalization (Bulò, Porzi, and Kortschieder 2024). For a fair comparison, we recompute the metrics with intended normalization for all models using the same normalization. We evaluate PSNR, SSIM, and LPIPS across all methods using identical hyperparameters and VGG backbone for LPIPS calculation.

Furthermore, the existing multi-scale Blender dataset (Mildenhall et al. 2021; Barron et al. 2021) performs box downsampling without accounting for the alpha, causing darkening artifacts at object boundaries. To resolve this issue, we incorporate alpha values into the box downsampling process, resulting in correct appearances at object boundaries regardless of background. Additionally, we note that unlike the multi-scale Blender dataset, the multi-scale Mip-NeRF 360 dataset (Barron et al. 2022) uses interpolation for downsampling. To better emulate real camera sensor behavior, we also apply box downsampling to the Mip-NeRF 360 dataset. For fair comparison, we retrain and evaluate all models using these consistently downsampled datasets.

For further implementation details, we refer readers to our code.

C Experiments

C.1 Experiment Setup

We run all experiments on a single NVIDIA RTX A6000 GPU with 48 GB of memory. The baseline models are trained and evaluated using their publicly available official codebases and default hyperparameters. For our proposed model, we individually validate each hyperparameter by comparing performance with values scaled by factors of $\times 2$ and $\times \frac{1}{2}$, selecting the hyperparameter value that yields the best or comparable performance. We run experiments for each combination of scene and resolution setting, and the reported metrics are averaged per scene and/or resolution.

C.2 Comparison with Supersampling

Supersampling is widely used to enhance rendering quality and reduce aliasing artifacts by first rendering scenes at

higher resolutions and then downsampling to the target resolution. Rendering at higher resolutions allows models to independently integrate alpha and transmittance values in 2D screen space, thus reducing the pixel-level dilation issues caused by scalar alpha blending. Nevertheless, supersampling significantly increases rendering time, posing a substantial drawback for real-time applications.

As shown qualitatively in Figure 9 and quantitatively in Table 6, our Gaussian Blending demonstrates superior effectiveness and efficiency compared to existing methods with supersampling such as 3DGS and Analytic-Splatting. Specifically, Analytic-Splatting requires at least 3×3 supersampling to achieve rendering quality comparable to our Gaussian Blending without supersampling, while 3DGS needs even higher levels of supersampling (over 5×5) for similar visual quality. Furthermore, our Gaussian Blending is at least three times faster than Analytic-Splatting with 3×3 supersampling and 3DGS with 5×5 supersampling, all while maintaining comparable or better rendering quality.

Remarkably, our Gaussian Blending achieves high-quality rendering without relying on supersampling, demonstrating clear suitability for real-time applications. Additionally, when employing 2×2 supersampling, Gaussian Blending can better handle the smaller splat case (in Figure 8(c)), achieving even higher rendering quality with a real-time rendering speed of 60 FPS.

C.3 Additional Results

In the main paper, to independently demonstrate zoom-out and zoom-in scenarios, we present results of models trained at the highest and lowest resolutions, respectively, and evaluate them in a multi-scale testing setting. However, our model shows superior rendering performance even when trained at arbitrary resolutions and also tested at arbitrary resolutions. As shown in Table 8 and Table 9, our model consistently achieves state-of-the-art results when simultaneously performing zoom-out and zoom-in by training at intermediate resolutions (e.g., 1/2 or 1/4 resolution) and evaluating at multiple scales. Moreover, our model also produces the highest rendering results when trained and tested at arbitrary sampling rates on the complex multi-scale Mip-NeRF 360 dataset (Table 12 - 15).

C.4 Limitations

Theoretically, the pinhole camera model should contain blurred appearance only when the object itself has smooth appearance, or when its edge is partially overlapping with the pixel. However, in Mip-NeRF 360 dataset, the real camera effects, such as diffraction, chromatic aberration, and defocus blur, cause inconsistent blur across different views as in Figure 10. Specifically, object edges are blurred across the pixels that are not even overlapping with the object. This negatively affects the scene reconstruction, where the inconsistent blur causes the splats to be misaligned with the object edges depending on the view. As a result, our model's performance gap in the multi-scale Mip-NeRF 360 dataset is not as large as in the multi-scale Blender dataset. However, our model still outperforms all other methods in the

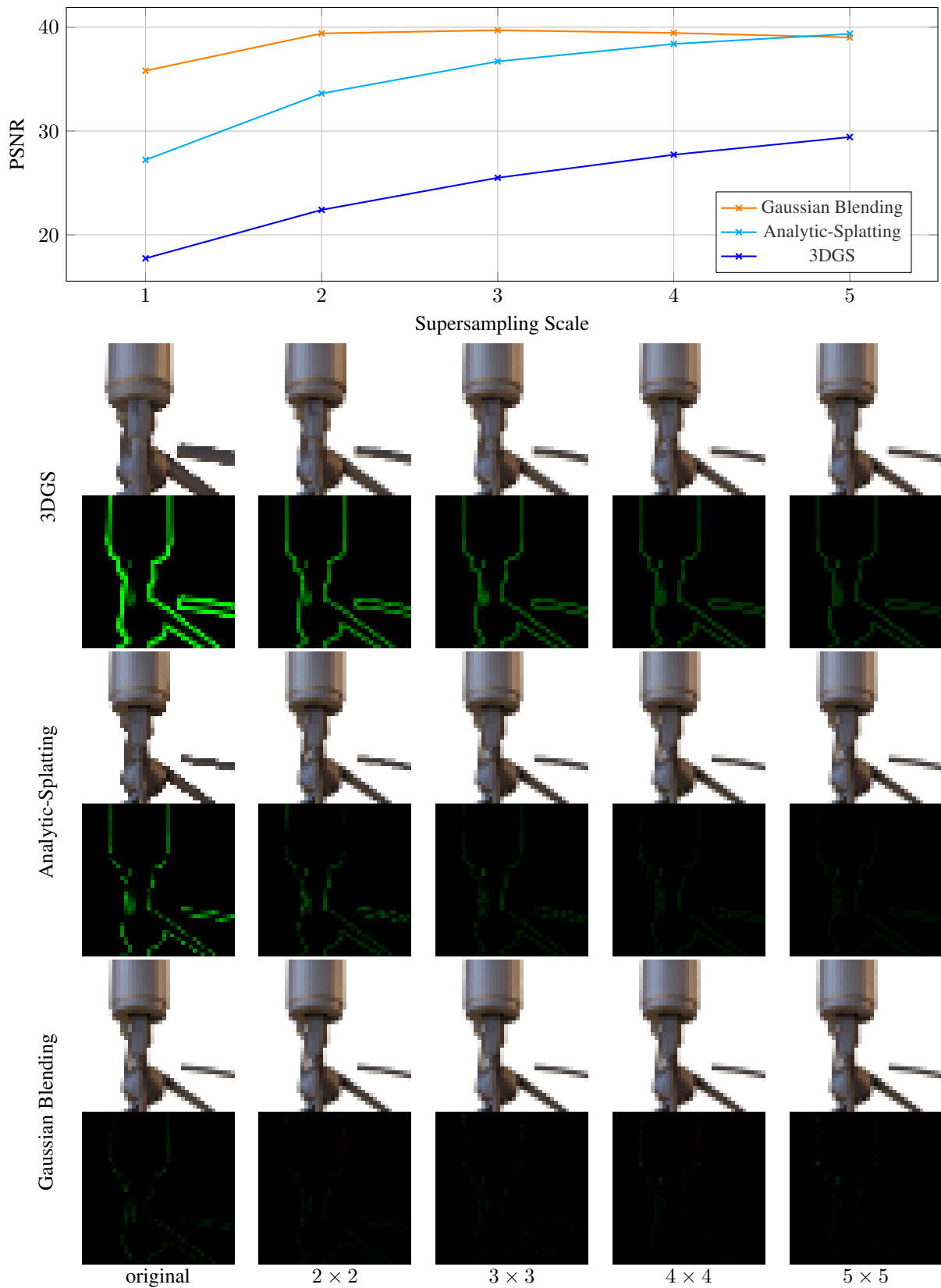


Figure 9: Comparison of supersampling results on the multi-scale Blender dataset trained at $\times 1$ resolution and rendered at $\times 1/8$ resolution. The dilated region is marked in green and the eroded region is marked in red.

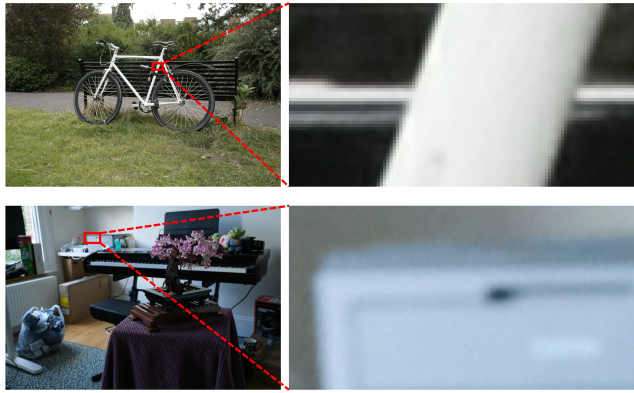


Figure 10: Due to the real camera effects, the Mip-NeRF 360 dataset contains inconsistent blur across different views.

Mip-NeRF 360 dataset, demonstrating its robustness to real camera effects.

We also observe that our model struggles to reconstruct highly specular objects when zooming in on the scene. Due to the ill-posed nature of the zoom-in task and the limited high-frequency information in the low-resolution training data, our model fails to accurately reconstruct the specular highlights as shown in Figure 11. However, our model still outperforms all other methods in this scenario, demonstrating its robustness to the zoom-in task.

We leave the improvement of real camera effects and zoom-in reconstruction of specular objects to future work, as these are orthogonal problems to our target of improving alpha blending to consider intra-pixel variations.

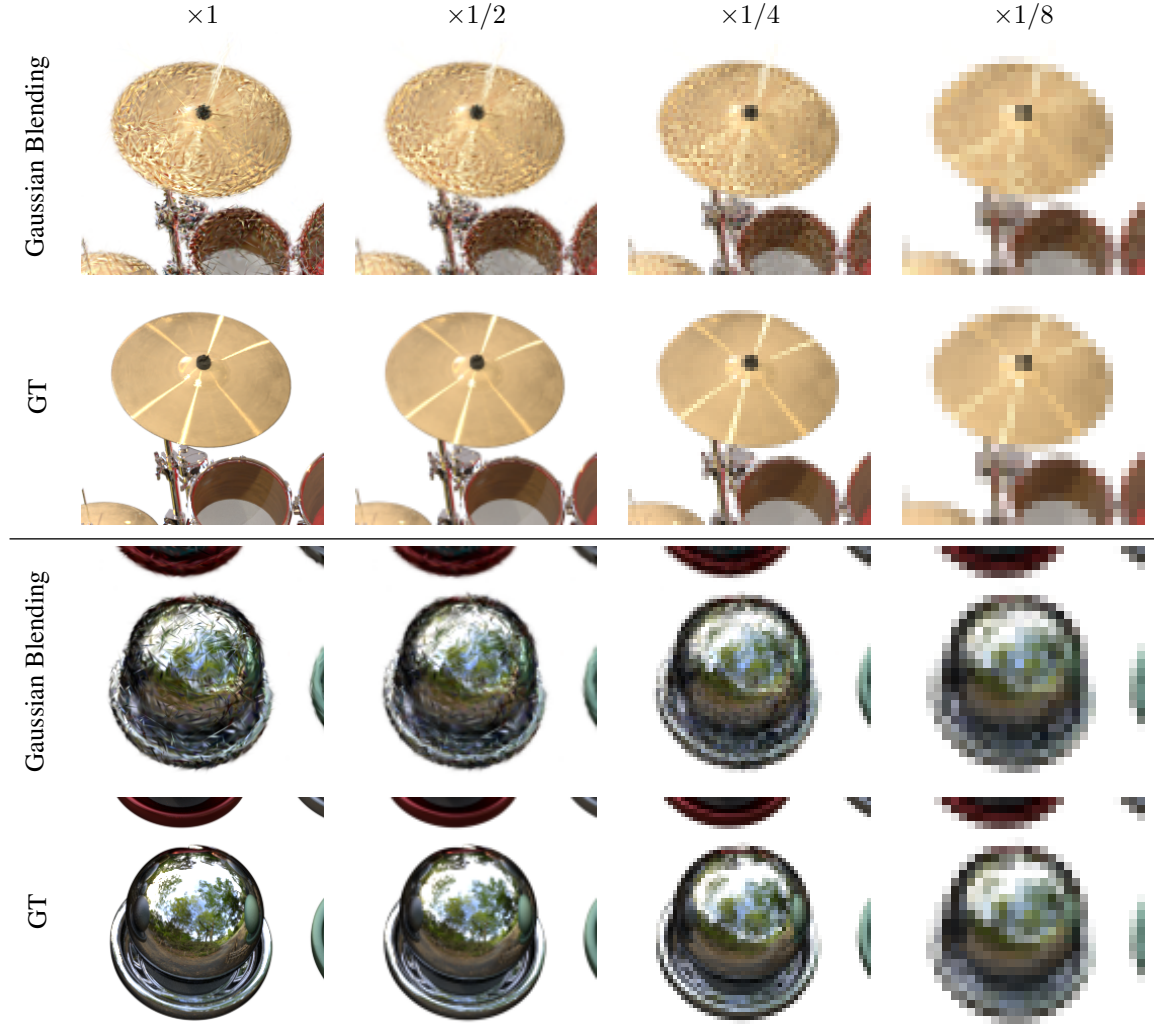


Figure 11: Example of failure cases when we try to zoom-in on the scene containing highly specular objects. Our model is trained at $\times 1/8$ resolution.

Table 6: Supersampling results on the multi-scale Blender dataset with single-scale training ($\times 1$ resolution) and multi-scale testing setting. Each model is represented with its supersampling scale.

	$\times 1$	$\times 1/2$	$\times 1/4$	$\times 1/8$	Avg.	$\times 1$	$\times 1/2$	$\times 1/4$	$\times 1/8$	Avg.	$\times 1$	$\times 1/2$	$\times 1/4$	$\times 1/8$	Avg.	FPS
3DGS	33.57	27.04	21.43	17.74	24.95	0.970	0.950	0.876	0.767	0.891	0.037	0.036	0.071	0.130	0.068	136.75
3DGS (2 \times 2)	33.86	31.47	26.53	22.41	28.57	0.971	0.972	0.952	0.906	0.950	0.036	0.024	0.035	0.064	0.040	81.05
3DGS (3 \times 3)	33.94	33.39	29.57	25.50	30.60	0.971	0.977	0.970	0.948	0.966	0.036	0.022	0.024	0.042	0.031	48.11
3DGS (4 \times 4)	33.94	34.32	31.55	27.72	31.88	0.971	0.978	0.977	0.965	0.973	0.036	0.021	0.019	0.031	0.027	30.84
3DGS (5 \times 5)	33.93	34.84	32.91	29.42	32.78	0.971	0.979	0.980	0.973	0.976	0.036	0.020	0.017	0.025	0.025	21.52
Analytic-Splatting	33.78	34.20	31.16	27.22	31.59	0.970	0.977	0.977	0.965	0.972	0.036	0.022	0.025	0.037	0.030	87.34
Analytic-Splatting (2 \times 2)	33.90	35.73	36.00	33.62	34.81	0.970	0.979	0.980	0.987	0.980	0.036	0.020	0.014	0.013	0.021	53.76
Analytic-Splatting (3 \times 3)	33.92	35.93	37.46	36.71	36.00	0.971	0.979	0.986	0.990	0.981	0.036	0.019	0.012	0.009	0.019	32.12
Analytic-Splatting (4 \times 4)	33.91	35.98	37.99	38.39	36.57	0.971	0.979	0.986	0.991	0.982	0.036	0.019	0.012	0.008	0.019	20.04
Analytic-Splatting (5 \times 5)	33.90	35.98	38.18	39.36	36.85	0.970	0.979	0.986	0.992	0.982	0.036	0.019	0.012	0.008	0.019	14.69
Gaussian Blending	33.91	35.78	36.81	35.81	35.58	0.970	0.979	0.985	0.989	0.981	0.027	0.020	0.013	0.012	0.020	99.26
Gaussian Blending (2 \times 2)	33.64	35.65	37.84	39.41	36.64	0.968	0.978	0.985	0.991	0.981	0.041	0.023	0.014	0.009	0.021	59.75
Gaussian Blending (3 \times 3)	33.21	35.15	37.44	39.71	36.38	0.966	0.976	0.984	0.991	0.979	0.046	0.026	0.016	0.009	0.024	34.12
Gaussian Blending (4 \times 4)	32.73	34.63	36.93	39.45	35.94	0.963	0.974	0.983	0.991	0.978	0.051	0.029	0.017	0.010	0.027	19.08
Gaussian Blending (5 \times 5)	32.24	34.09	36.40	39.02	35.44	0.960	0.972	0.982	0.990	0.976	0.056	0.032	0.019	0.011	0.029	12.37

Table 7: Single-scale training ($\times 1$ resolution) and multi-scale testing results on the multi-scale Blender dataset. The best results are highlighted in **bold**.

	PSNR \uparrow					SSIM \uparrow					LPIPS \downarrow				
	$\times 1$	$\times 1/2$	$\times 1/4$	$\times 1/8$	Avg.	$\times 1$	$\times 1/2$	$\times 1/4$	$\times 1/8$	Avg.	$\times 1$	$\times 1/2$	$\times 1/4$	$\times 1/8$	Avg.
TensoRF	33.22	33.27	30.23	26.77	30.87	0.964	0.972	0.968	0.953	0.964	0.047	0.034	0.049	0.079	0.052
3DGS	33.57	27.04	21.43	17.74	24.95	0.970	0.950	0.876	0.767	0.891	0.037	0.036	0.071	0.130	0.068
Scaffold-GS	31.76	27.46	22.14	18.34	24.92	0.961	0.949	0.886	0.784	0.895	0.050	0.041	0.067	0.121	0.070
2DGS	31.81	26.73	20.21	16.41	23.79	0.965	0.946	0.846	0.711	0.867	0.048	0.052	0.102	0.177	0.095
3D-HGS	33.70	27.34	21.71	17.99	25.19	0.970	0.953	0.883	0.777	0.896	0.037	0.035	0.067	0.124	0.066
Tri-MipRF	32.86	32.80	28.44	24.22	29.58	0.959	0.968	0.955	0.924	0.951	0.056	0.039	0.051	0.075	0.055
3DGS+EWA	33.60	32.05	28.28	25.11	29.76	0.970	0.972	0.963	0.946	0.962	0.039	0.027	0.033	0.045	0.036
3DGS+SS	33.86	31.47	26.53	22.41	28.57	0.971	0.972	0.952	0.906	0.950	0.036	0.024	0.035	0.064	0.040
Mip-Splatting	33.54	34.09	31.50	27.80	31.73	0.969	0.976	0.977	0.968	0.973	0.038	0.022	0.022	0.032	0.028
Analytic-Splatting	33.78	34.20	31.16	27.22	31.59	0.970	0.977	0.977	0.965	0.972	0.036	0.022	0.025	0.037	0.030
Scaffold-GS+GB	30.22	32.02	33.84	33.80	32.47	0.949	0.964	0.976	0.983	0.968	0.070	0.041	0.025	0.019	0.039
2DGS+GB	31.96	33.53	34.93	34.74	33.79	0.960	0.970	0.979	0.985	0.974	0.055	0.033	0.022	0.015	0.031
Mip-Splatting+GB _{test}	33.45	35.37	36.98	36.36	35.54	0.969	0.978	0.984	0.988	0.980	0.038	0.021	0.014	0.012	0.021
Analytic-Splatting+GB _{test}	33.62	35.72	37.36	36.51	35.80	0.970	0.979	0.985	0.989	0.981	0.037	0.020	0.013	0.011	0.020
Gaussian Blending	33.92	35.80	36.82	35.79	35.58	0.970	0.979	0.985	0.988	0.981	0.036	0.020	0.013	0.012	0.020

Table 8: Single-scale training ($\times 1/2$ resolution) and multi-scale testing results on the multi-scale Blender dataset. The best results are highlighted in **bold**.

	PSNR \uparrow					SSIM \uparrow					LPIPS \downarrow				
	$\times 1$	$\times 1/2$	$\times 1/4$	$\times 1/8$	Avg.	$\times 1$	$\times 1/2$	$\times 1/4$	$\times 1/8$	Avg.	$\times 1$	$\times 1/2$	$\times 1/4$	$\times 1/8$	Avg.
TensoRF	31.83	34.11	32.03	27.84	31.45	0.956	0.972	0.974	0.961	0.966	0.062	0.033	0.037	0.066	0.049
3DGS	26.66	34.08	24.62	19.04	26.10	0.937	0.975	0.930	0.814	0.914	0.058	0.023	0.045	0.103	0.058
Scaffold-GS	26.37	32.72	24.81	19.43	25.84	0.928	0.969	0.931	0.824	0.913	0.075	0.033	0.046	0.098	0.063
2DGS	29.03	32.38	23.49	17.52	25.61	0.949	0.970	0.915	0.760	0.898	0.064	0.033	0.062	0.140	0.075
3D-HGS	27.03	34.34	24.83	19.20	26.35	0.938	0.975	0.934	0.820	0.917	0.059	0.023	0.043	0.100	0.056
Tri-MipRF	30.66	33.82	30.48	25.59	30.14	0.943	0.969	0.965	0.939	0.954	0.082	0.038	0.040	0.063	0.056
3DGS+EWA	29.41	33.99	30.50	26.24	30.03	0.950	0.975	0.973	0.956	0.963	0.059	0.026	0.026	0.039	0.038
3DGS+SS	29.88	35.12	29.30	23.73	29.51	0.956	0.978	0.969	0.926	0.957	0.048	0.021	0.024	0.052	0.036
Mip-Splatting	31.64	34.16	33.31	29.06	32.04	0.960	0.975	0.980	0.974	0.972	0.052	0.024	0.018	0.027	0.030
Analytic-Splatting	31.91	34.89	33.24	28.46	32.13	0.961	0.977	0.981	0.972	0.973	0.049	0.022	0.019	0.031	0.030
Scaffold-GS+GB	30.06	32.06	34.29	34.39	32.70	0.945	0.963	0.977	0.985	0.968	0.078	0.042	0.024	0.017	0.040
2DGS+GB	29.90	32.42	34.35	34.56	32.81	0.943	0.964	0.977	0.984	0.967	0.074	0.039	0.023	0.015	0.038
Mip-Splatting+GB _{test}	31.48	33.74	36.26	36.94	34.60	0.960	0.975	0.983	0.989	0.977	0.053	0.025	0.014	0.011	0.026
Analytic-Splatting+GB _{test}	31.63	34.31	37.10	37.87	35.23	0.959	0.976	0.985	0.990	0.978	0.050	0.023	0.013	0.009	0.024
Gaussian Blending	32.51	35.24	37.15	36.13	35.26	0.962	0.977	0.985	0.989	0.978	0.046	0.021	0.013	0.011	0.023

Table 9: Single-scale training ($\times 1/4$ resolution) and multi-scale testing results on the multi-scale Blender dataset. The best results are highlighted in **bold**.

	PSNR \uparrow					SSIM \uparrow					LPIPS \downarrow				
	$\times 1$	$\times 1/2$	$\times 1/4$	$\times 1/8$	Avg.	$\times 1$	$\times 1/2$	$\times 1/4$	$\times 1/8$	Avg.	$\times 1$	$\times 1/2$	$\times 1/4$	$\times 1/8$	Avg.
TensoRF	28.51	30.54	33.73	30.49	30.82	0.922	0.951	0.974	0.972	0.955	0.111	0.070	0.032	0.044	0.064
3DGS	21.56	24.76	34.49	22.70	25.88	0.866	0.920	0.979	0.908	0.918	0.114	0.061	0.019	0.059	0.063
Scaffold-GS	20.73	23.83	33.71	22.38	25.16	0.854	0.904	0.975	0.904	0.909	0.132	0.079	0.025	0.060	0.074
2DGS	25.70	27.23	32.37	21.14	26.61	0.910	0.937	0.971	0.875	0.923	0.109	0.069	0.032	0.083	0.074
3D-HGS	22.00	25.07	34.88	22.73	26.17	0.870	0.922	0.979	0.910	0.920	0.117	0.061	0.018	0.057	0.063
Tri-MipRF	26.19	28.12	34.18	28.44	29.23	0.887	0.925	0.976	0.962	0.937	0.147	0.104	0.028	0.044	0.081
3DGS+EWA	24.64	27.80	34.35	29.07	28.97	0.894	0.944	0.979	0.972	0.947	0.112	0.057	0.022	0.028	0.055
3DGS+SS	24.68	28.12	36.11	27.32	29.06	0.906	0.950	0.982	0.962	0.950	0.086	0.042	0.015	0.030	0.043
Mip-Splatting	28.68	30.79	34.81	32.26	31.63	0.934	0.959	0.980	0.983	0.964	0.088	0.048	0.019	0.017	0.043
Analytic-Splatting	28.58	31.16	35.69	31.57	31.75	0.928	0.959	0.981	0.982	0.962	0.090	0.045	0.017	0.020	0.043
Scaffold-GS+GB	28.78	30.72	33.98	35.35	32.21	0.916	0.946	0.973	0.986	0.955	0.112	0.071	0.030	0.015	0.057
2DGS+GB	27.56	29.65	32.61	34.20	31.00	0.916	0.943	0.967	0.981	0.951	0.112	0.069	0.035	0.019	0.059
Mip-Splatting+GB _{test}	28.62	30.48	33.72	36.64	32.36	0.933	0.959	0.979	0.989	0.965	0.089	0.050	0.019	0.010	0.042
Analytic-Splatting+GB _{test}	28.44	30.74	34.20	37.64	32.76	0.926	0.958	0.979	0.990	0.963	0.091	0.047	0.018	0.009	0.041
Gaussian Blending	29.70	32.37	36.30	37.33	33.92	0.936	0.964	0.982	0.990	0.968	0.082	0.040	0.016	0.009	0.037

Table 10: Single-scale training ($\times 1/8$ resolution) and multi-scale testing results on the multi-scale Blender dataset. The best results are highlighted in **bold**.

	PSNR \uparrow						SSIM \uparrow						LPIPS \downarrow					
	$\times 1$	$\times 1/2$	$\times 1/4$	$\times 1/8$	Avg.		$\times 1$	$\times 1/2$	$\times 1/4$	$\times 1/8$	Avg.		$\times 1$	$\times 1/2$	$\times 1/4$	$\times 1/8$	Avg.	
TensoRF	25.42	26.57	29.02	32.87	28.47	0.874	0.902	0.946	0.977	0.925	0.159	0.132	0.078	0.028	0.099			
3DGS	18.51	19.90	23.33	34.72	24.11	0.824	0.832	0.905	0.984	0.886	0.163	0.136	0.072	0.016	0.097			
Scaffold-GS	16.37	17.71	21.35	34.06	22.37	0.802	0.797	0.867	0.980	0.862	0.187	0.172	0.106	0.020	0.121			
2DGS	22.87	23.59	25.46	31.85	25.94	0.864	0.879	0.920	0.973	0.909	0.159	0.139	0.087	0.031	0.104			
3D-HGS	18.87	20.16	23.39	35.08	24.38	0.826	0.834	0.904	0.984	0.887	0.169	0.142	0.073	0.015	0.100			
Tri-MipRF	21.99	22.91	25.84	33.93	26.17	0.809	0.821	0.888	0.979	0.874	0.240	0.232	0.170	0.023	0.166			
3DGS+EWA	21.76	23.15	26.64	34.32	26.47	0.834	0.871	0.938	0.983	0.907	0.231	0.184	0.095	0.019	0.132			
3DGS+SS	20.98	22.47	26.33	36.96	26.68	0.851	0.877	0.942	0.987	0.914	0.136	0.100	0.048	0.012	0.074			
Mip-Splatting	25.97	27.24	30.06	35.29	29.64	0.892	0.920	0.959	0.985	0.939	0.150	0.117	0.056	0.015	0.084			
Analytic-Splatting	25.45	26.98	30.04	35.63	29.53	0.878	0.914	0.956	0.984	0.933	0.138	0.102	0.051	0.015	0.077			
Scaffold-GS+GB	26.57	28.02	31.11	35.92	30.41	0.886	0.918	0.958	0.985	0.937	0.149	0.116	0.061	0.016	0.085			
2DGS+GB	25.49	26.94	29.47	33.05	28.74	0.880	0.908	0.947	0.976	0.928	0.151	0.120	0.067	0.025	0.091			
Mip-Splatting+GB _{test}	25.95	27.17	29.67	33.69	29.12	0.891	0.919	0.958	0.984	0.938	0.151	0.120	0.059	0.016	0.087			
Analytic-Splatting+GB _{test}	25.37	26.87	29.51	33.34	28.78	0.876	0.912	0.954	0.982	0.931	0.139	0.104	0.053	0.017	0.078			
Gaussian Blending	26.74	28.53	31.97	36.92	31.04	0.891	0.927	0.965	0.987	0.943	0.132	0.092	0.042	0.012	0.069			

Table 11: Multi-scale training and multi-scale testing results on the multi-scale Blender dataset. The best results are highlighted in **bold**.

	PSNR \uparrow						SSIM \uparrow						LPIPS \downarrow					
	$\times 1$	$\times 1/2$	$\times 1/4$	$\times 1/8$	Avg.		$\times 1$	$\times 1/2$	$\times 1/4$	$\times 1/8$	Avg.		$\times 1$	$\times 1/2$	$\times 1/4$	$\times 1/8$	Avg.	
TensoRF	33.03	33.92	30.99	27.26	31.30	0.963	0.973	0.971	0.957	0.966	0.049	0.032	0.043	0.073	0.049			
3DGS	30.19	31.38	30.59	27.05	29.90	0.954	0.967	0.968	0.950	0.960	0.061	0.037	0.031	0.041	0.042			
Scaffold-GS	28.56	29.85	29.41	26.08	28.48	0.938	0.955	0.961	0.940	0.948	0.085	0.054	0.041	0.054	0.058			
2DGS	27.95	29.39	30.31	26.23	28.47	0.934	0.954	0.965	0.942	0.949	0.094	0.063	0.044	0.059	0.065			
3D-HGS	30.96	32.40	31.90	28.70	30.99	0.957	0.970	0.973	0.963	0.966	0.056	0.032	0.025	0.032	0.036			
Tri-MipRF	32.60	34.18	34.97	35.32	34.27	0.958	0.971	0.980	0.987	0.974	0.057	0.033	0.022	0.015	0.032			
3DGS+EWA	30.34	31.78	32.45	31.50	31.52	0.952	0.967	0.976	0.979	0.968	0.068	0.039	0.028	0.026	0.040			
3DGS+SS	32.12	33.81	33.98	31.13	32.76	0.965	0.976	0.980	0.977	0.974	0.046	0.025	0.018	0.021	0.027			
Mip-Splatting	32.93	34.68	35.79	35.48	34.72	0.967	0.977	0.983	0.988	0.979	0.041	0.022	0.015	0.012	0.023			
Analytic-Splatting	33.28	35.02	36.07	35.90	35.07	0.968	0.978	0.984	0.989	0.980	0.040	0.022	0.014	0.011	0.022			
Scaffold-GS+GB	29.68	31.56	33.81	34.87	32.48	0.944	0.961	0.975	0.985	0.966	0.079	0.046	0.028	0.018	0.043			
2DGS+GB	31.12	32.89	34.99	36.26	33.81	0.954	0.967	0.979	0.987	0.972	0.064	0.037	0.021	0.013	0.034			
Mip-Splatting+GB _{test}	32.85	34.69	36.32	37.00	35.22	0.967	0.977	0.984	0.990	0.979	0.042	0.022	0.014	0.009	0.022			
Analytic-Splatting+GB _{test}	33.15	35.09	36.52	36.44	35.30	0.968	0.978	0.985	0.990	0.980	0.041	0.022	0.013	0.009	0.021			
Gaussian Blending	33.50	35.48	37.38	38.39	36.19	0.968	0.978	0.985	0.991	0.981	0.040	0.021	0.013	0.009	0.021			

Table 12: Single-scale training ($\times 1$ resolution) and multi-scale testing results on the multi-scale Mip-NeRF 360 dataset. The best results are highlighted in **bold**.

	PSNR \uparrow						SSIM \uparrow						LPIPS \downarrow					
	$\times 1$	$\times 1/2$	$\times 1/4$	$\times 1/8$	Avg.		$\times 1$	$\times 1/2$	$\times 1/4$	$\times 1/8$	Avg.		$\times 1$	$\times 1/2$	$\times 1/4$	$\times 1/8$	Avg.	
3DGS	27.63	25.76	21.98	19.34	23.68	0.820	0.815	0.703	0.570	0.727	0.259	0.208	0.231	0.268	0.242			
Scaffold-GS	27.27	26.05	22.48	19.70	23.87	0.804	0.812	0.712	0.583	0.728	0.284	0.216	0.219	0.254	0.243			
2DGS	26.71	25.99	21.84	18.41	23.24	0.795	0.804	0.671	0.491	0.690	0.309	0.235	0.262	0.327	0.283			
3D-HGS	28.07	26.12	22.13	19.36	23.92	0.823	0.823	0.712	0.578	0.734	0.250	0.198	0.222	0.258	0.232			
3DGS+EWA	27.67	28.40	28.23	27.19	27.87	0.819	0.858	0.879	0.887	0.861	0.266	0.185	0.139	0.118	0.177			
3DGS+SS	27.67	27.71	25.47	22.59	25.86	0.820	0.854	0.831	0.757	0.816	0.258	0.179	0.159	0.180	0.194			
Mip-Splatting	27.50	28.27	29.22	28.89	28.47	0.825	0.867	0.907	0.922	0.880	0.234	0.146	0.088	0.070	0.135			
Analytic-Splatting	27.36	28.12	28.92	28.51	28.23	0.811	0.855	0.897	0.914	0.869	0.264	0.176	0.111	0.085	0.159			
Gaussian Blending	27.55	28.62	29.92	30.58	29.17	0.829	0.875	0.915	0.936	0.889	0.232	0.150	0.095	0.069	0.137			

Table 13: Single-scale training ($\times 1/2$ resolution) and multi-scale testing results on the multi-scale Mip-NeRF 360 dataset. The best results are highlighted in **bold**.

	PSNR \uparrow					SSIM \uparrow					LPIPS \downarrow				
	$\times 1$	$\times 1/2$	$\times 1/4$	$\times 1/8$	Avg.	$\times 1$	$\times 1/2$	$\times 1/4$	$\times 1/8$	Avg.	$\times 1$	$\times 1/2$	$\times 1/4$	$\times 1/8$	Avg.
3DGS	24.50	28.55	24.47	20.53	24.51	0.749	0.864	0.810	0.650	0.768	0.323	0.169	0.169	0.227	0.222
Scaffold-GS	25.03	28.41	24.71	20.72	24.72	0.740	0.853	0.812	0.657	0.765	0.340	0.185	0.165	0.217	0.227
2DGS	26.06	27.85	24.59	19.89	24.60	0.760	0.845	0.791	0.582	0.744	0.342	0.201	0.186	0.274	0.251
3D-HGS	24.85	29.06	24.73	20.62	24.82	0.753	0.866	0.818	0.657	0.773	0.312	0.162	0.160	0.219	0.213
3DGS+EWA	26.28	28.53	28.93	27.90	27.91	0.767	0.859	0.894	0.899	0.854	0.331	0.186	0.124	0.108	0.187
3DGS+SS	26.35	28.72	27.19	23.58	26.46	0.782	0.866	0.876	0.799	0.831	0.298	0.164	0.124	0.155	0.185
Mip-Splatting	26.94	28.44	29.60	29.52	28.62	0.793	0.863	0.911	0.929	0.874	0.272	0.156	0.085	0.064	0.144
Analytic-Splatting	26.56	28.42	29.59	29.36	28.48	0.767	0.854	0.907	0.927	0.864	0.306	0.171	0.097	0.071	0.161
Gaussian Blending	27.40	28.66	30.14	31.07	29.32	0.814	0.873	0.919	0.942	0.887	0.254	0.146	0.084	0.059	0.136

Table 14: Single-scale training ($\times 1/4$ resolution) and multi-scale testing results on the multi-scale Mip-NeRF 360 dataset. The best results are highlighted in **bold**.

	PSNR \uparrow					SSIM \uparrow					LPIPS \downarrow				
	$\times 1$	$\times 1/2$	$\times 1/4$	$\times 1/8$	Avg.	$\times 1$	$\times 1/2$	$\times 1/4$	$\times 1/8$	Avg.	$\times 1$	$\times 1/2$	$\times 1/4$	$\times 1/8$	Avg.
3DGS	19.89	23.11	29.67	23.90	24.14	0.575	0.734	0.903	0.809	0.755	0.462	0.279	0.105	0.148	0.248
Scaffold-GS	20.50	23.39	29.78	23.65	24.33	0.569	0.723	0.899	0.807	0.750	0.470	0.289	0.109	0.145	0.253
2DGS	23.59	25.08	28.80	23.45	25.23	0.650	0.747	0.883	0.769	0.762	0.438	0.300	0.130	0.177	0.261
3D-HGS	20.60	23.70	30.27	24.10	24.67	0.587	0.742	0.905	0.815	0.762	0.448	0.264	0.099	0.141	0.238
3DGS+EWA	22.89	25.59	29.35	29.01	26.71	0.615	0.767	0.893	0.915	0.797	0.445	0.287	0.126	0.094	0.238
3DGS+SS	22.89	25.49	29.98	26.45	26.20	0.665	0.789	0.908	0.886	0.812	0.408	0.237	0.098	0.102	0.211
Mip-Splatting	26.03	27.43	29.79	30.64	28.47	0.718	0.814	0.905	0.939	0.844	0.359	0.230	0.096	0.056	0.185
Analytic-Splatting	25.01	26.88	29.74	30.49	28.03	0.672	0.791	0.899	0.938	0.825	0.409	0.235	0.101	0.060	0.201
Gaussian Blending	26.44	27.75	29.78	31.25	28.80	0.747	0.833	0.910	0.945	0.859	0.339	0.206	0.092	0.055	0.173

Table 15: Single-scale training ($\times 1/8$ resolution) and multi-scale testing results on the multi-scale Mip-NeRF 360 dataset. The best results are highlighted in **bold**.

	PSNR \uparrow					SSIM \uparrow					LPIPS \downarrow				
	$\times 1$	$\times 1/2$	$\times 1/4$	$\times 1/8$	Avg.	$\times 1$	$\times 1/2$	$\times 1/4$	$\times 1/8$	Avg.	$\times 1$	$\times 1/2$	$\times 1/4$	$\times 1/8$	Avg.
3DGS	17.25	18.73	22.41	30.60	22.25	0.452	0.516	0.726	0.930	0.656	0.566	0.463	0.245	0.071	0.336
Scaffold-GS	17.09	18.43	21.98	31.06	22.14	0.443	0.490	0.705	0.932	0.643	0.576	0.477	0.262	0.068	0.346
2DGS	20.92	21.66	23.85	29.49	23.98	0.533	0.580	0.728	0.910	0.688	0.544	0.457	0.276	0.093	0.342
3D-HGS	18.16	19.59	23.10	31.26	23.03	0.466	0.529	0.738	0.931	0.666	0.560	0.451	0.232	0.067	0.327
3DGS+EWA	20.27	21.76	24.90	29.38	24.08	0.466	0.573	0.765	0.904	0.677	0.541	0.443	0.259	0.105	0.337
3DGS+SS	20.14	21.50	24.84	31.22	24.42	0.535	0.624	0.802	0.937	0.725	0.514	0.390	0.189	0.063	0.289
Mip-Splatting	24.35	25.51	27.79	30.95	27.15	0.603	0.695	0.838	0.934	0.768	0.481	0.369	0.192	0.064	0.277
Analytic-Splatting	23.00	24.37	27.12	30.86	26.34	0.545	0.655	0.817	0.930	0.737	0.508	0.385	0.186	0.065	0.286
Gaussian Blending	24.86	25.97	28.13	30.90	27.47	0.632	0.720	0.849	0.935	0.784	0.464	0.345	0.178	0.065	0.263

Table 16: Multi-scale training and multi-scale testing results on the multi-scale Mip-NeRF 360 dataset. The best results are highlighted in **bold**.

	PSNR \uparrow					SSIM \uparrow					LPIPS \downarrow				
	$\times 1$	$\times 1/2$	$\times 1/4$	$\times 1/8$	Avg.	$\times 1$	$\times 1/2$	$\times 1/4$	$\times 1/8$	Avg.	$\times 1$	$\times 1/2$	$\times 1/4$	$\times 1/8$	Avg.
3DGS	26.85	27.89	28.28	27.17	27.55	0.790	0.847	0.882	0.876	0.849	0.311	0.205	0.132	0.111	0.190
Scaffold-GS	26.61	27.75	28.42	27.23	27.50	0.773	0.835	0.879	0.875	0.841	0.333	0.223	0.136	0.112	0.201
2DGS	25.70	26.73	27.72	26.52	26.67	0.729	0.799	0.860	0.856	0.811	0.392	0.278	0.162	0.135	0.242
3D-HGS	27.47	28.62	29.40	28.75	28.56	0.800	0.857	0.897	0.904	0.864	0.293	0.188	0.115	0.090	0.171
3DGS+EWA	26.50	27.75	28.93	29.25	28.11	0.763	0.831	0.887	0.918	0.850	0.330	0.221	0.139	0.095	0.196
3DGS+SS	27.37	28.54	29.69	29.44	28.76	0.807	0.864	0.909	0.922	0.876	0.287	0.180	0.104	0.078	0.162
Mip-Splatting	27.41	28.46	30.01	31.13	29.25	0.816	0.868	0.916	0.943	0.886	0.253	0.153	0.083	0.052	0.135
Analytic-Splatting	27.31	28.40	29.98	31.17	29.21	0.804	0.860	0.913	0.945	0.880	0.277	0.175	0.096	0.056	0.151
Gaussian Blending	27.58	28.77	30.24	31.54	29.53	0.827	0.877	0.921	0.948	0.893	0.237	0.146	0.085	0.054	0.130



Figure 12: Qualitative results of single-scale training ($\times 1$ resolution) and multi-scale testing setting on the multi-scale Blender dataset. The training resolution is highlighted in **bold**.

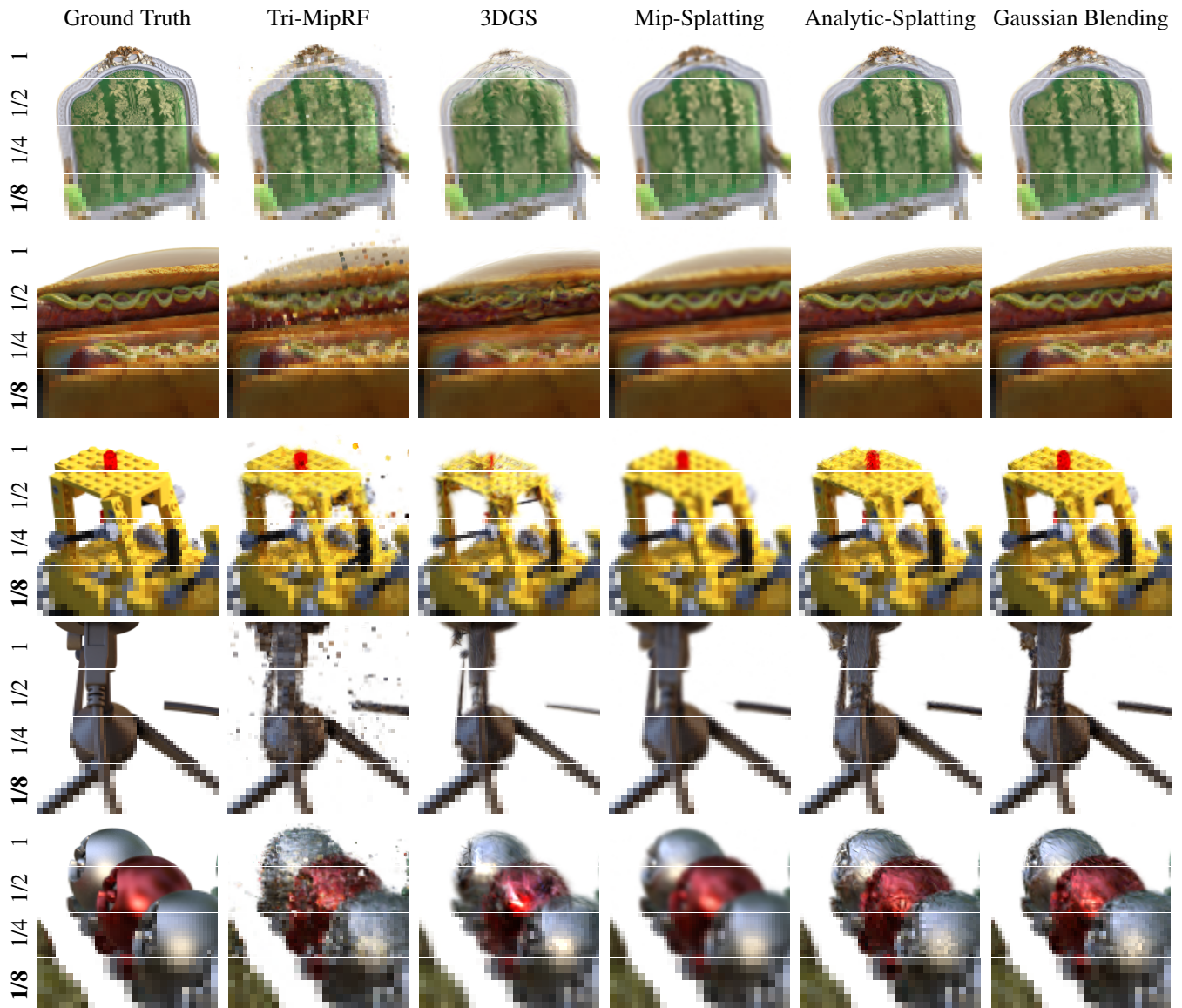


Figure 13: Qualitative results of single-scale training ($\times 1/8$ resolution) and multi-scale testing setting on the multi-scale Blender dataset. The training resolution is highlighted in **bold**.

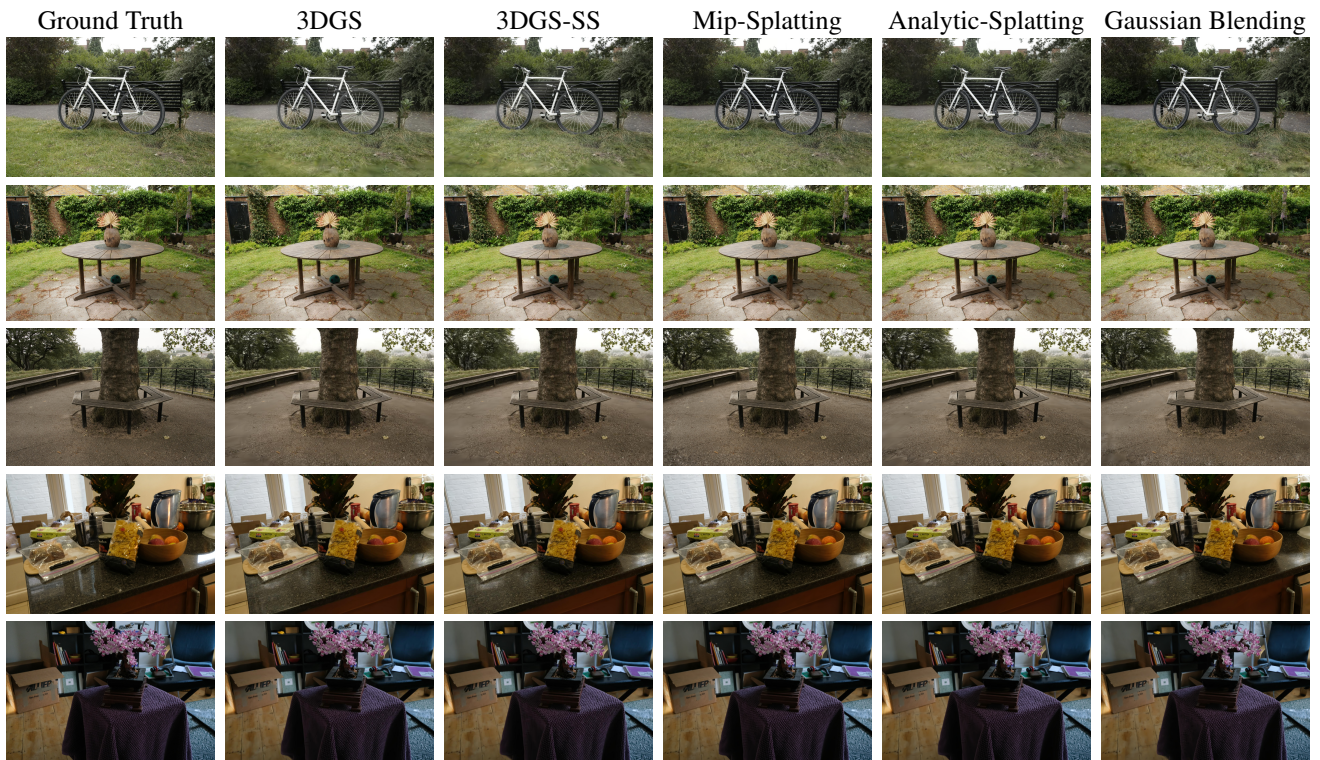


Figure 14: Qualitative results of Novel View Synthesis (NVS) setting on the multi-scale Mip-NeRF 360 dataset.



Figure 15: Qualitative results of zoom-out setting on the multi-scale Blender dataset. The training resolution and rendering resolution is represented as (training resolution) \rightarrow (rendering resolution).

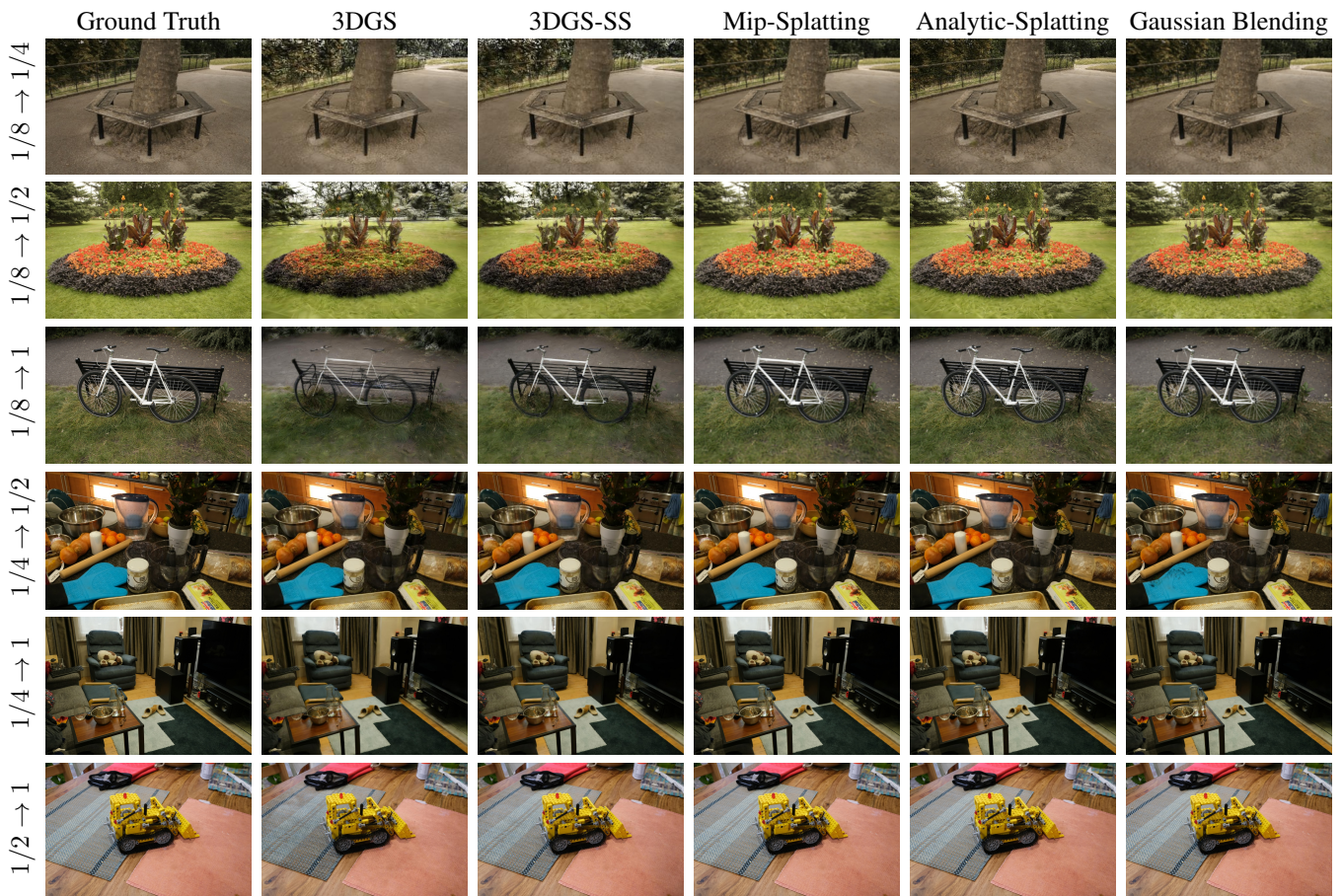


Figure 16: Qualitative results of zoom-in setting on the multi-scale Mip-NeRF 360 dataset. The training resolution and rendering resolution is represented as (training resolution) \rightarrow (rendering resolution).

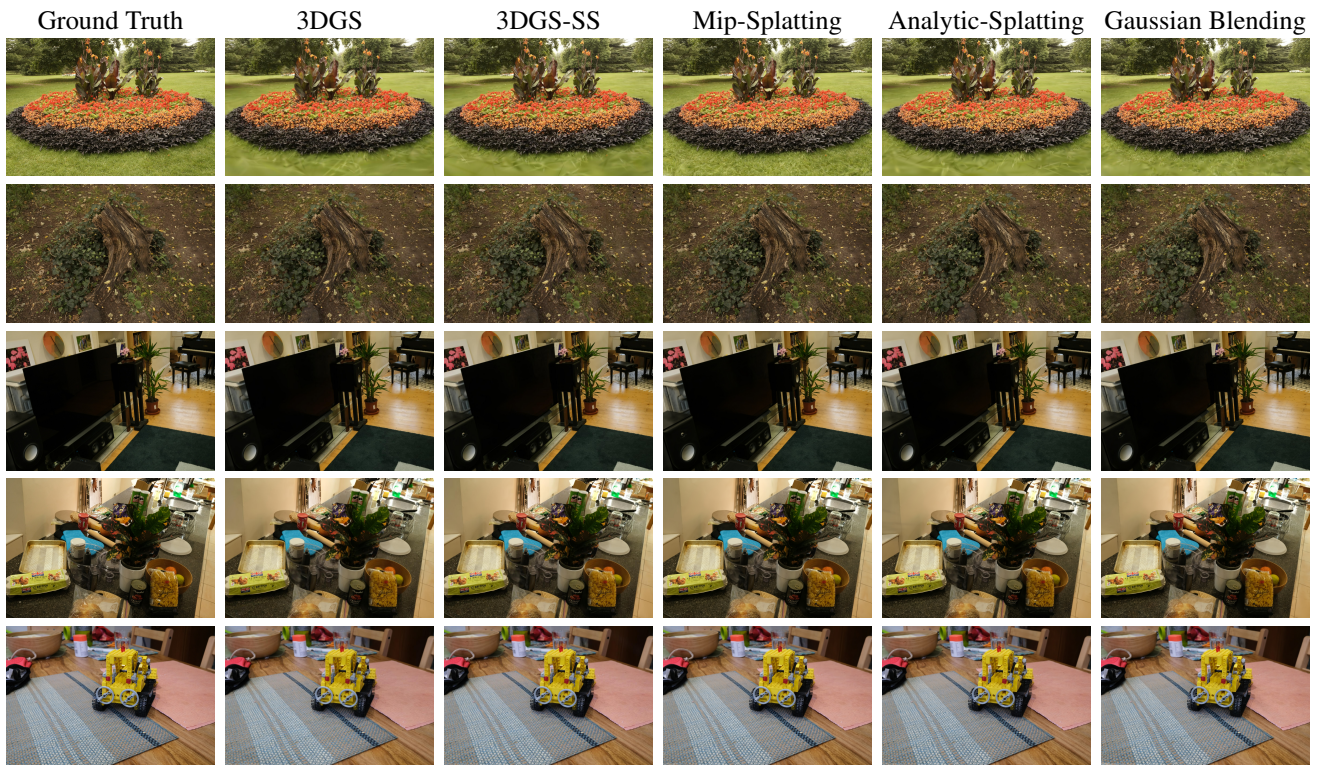


Figure 17: Qualitative results of multi-scale training and multi-scale testing on the multi-scale Mip-NeRF 360 dataset. All images are rendered at $\times 1$ resolution.

Table 17: Single-scale training ($\times 1$ resolution) and multi-scale testing results on the multi-scale Blender dataset. The best results are highlighted in **bold**.

	chair	drums	ficus	hotdog	lego	materials	mic	ship	Avg.
TensoRF	32.57	25.63	31.70	35.16	32.05	28.80	31.77	29.30	30.87
3DGS	26.59	21.24	26.25	28.85	25.59	23.06	24.81	23.15	24.94
Scaffold-GS	26.82	21.14	25.93	29.62	25.33	23.36	24.28	22.93	24.92
2DGS	23.04	20.52	25.99	28.25	24.47	22.61	22.75	22.69	23.79
3D-HGS	26.74	21.53	26.33	29.27	25.71	23.38	25.19	23.34	25.19
Tri-MipRF	32.61	24.11	28.09	34.94	30.67	28.05	31.08	27.09	29.58
3DGS+EWA	33.17	25.05	31.95	33.55	30.12	27.70	28.57	27.98	29.76
3DGS+SS	29.67	24.18	30.07	33.05	29.73	26.57	29.22	26.07	28.57
Mip-Splatting	35.56	26.13	32.95	35.67	32.77	29.83	31.42	29.54	31.73
Analytic-Splatting	35.37	25.84	33.36	35.66	32.39	29.24	31.23	29.62	31.59
Gaussian Blending	39.10	28.05	37.39	39.98	37.17	32.40	37.84	32.74	35.58
	chair	drums	ficus	hotdog	lego	materials	mic	ship	Avg.
TensoRF	0.975	0.941	0.980	0.982	0.974	0.964	0.982	0.914	0.964
3DGS	0.914	0.850	0.920	0.931	0.887	0.882	0.913	0.829	0.891
Scaffold-GS	0.918	0.847	0.922	0.948	0.892	0.893	0.910	0.828	0.895
2DGS	0.879	0.821	0.908	0.915	0.864	0.863	0.879	0.805	0.867
3D-HGS	0.917	0.856	0.921	0.936	0.891	0.889	0.920	0.835	0.896
Tri-MipRF	0.978	0.915	0.959	0.978	0.963	0.956	0.977	0.884	0.951
3DGS+EWA	0.980	0.942	0.983	0.979	0.967	0.961	0.970	0.919	0.963
3DGS+SS	0.964	0.926	0.967	0.975	0.959	0.948	0.971	0.891	0.950
Mip-Splatting	0.989	0.955	0.987	0.986	0.983	0.974	0.984	0.922	0.973
Analytic-Splatting	0.988	0.952	0.988	0.986	0.980	0.971	0.984	0.929	0.972
Gaussian Blending	0.993	0.965	0.994	0.991	0.991	0.979	0.995	0.938	0.981
	chair	drums	ficus	hotdog	lego	materials	mic	ship	Avg.
TensoRF	0.040	0.073	0.028	0.036	0.037	0.058	0.039	0.105	0.052
3DGS	0.051	0.095	0.056	0.042	0.068	0.060	0.048	0.128	0.069
Scaffold-GS	0.051	0.099	0.057	0.038	0.067	0.057	0.053	0.136	0.070
2DGS	0.109	0.120	0.069	0.058	0.086	0.070	0.090	0.156	0.095
3D-HGS	0.051	0.089	0.055	0.040	0.065	0.057	0.044	0.124	0.066
Tri-MipRF	0.026	0.090	0.042	0.029	0.039	0.055	0.029	0.131	0.055
3DGS+EWA	0.021	0.054	0.019	0.021	0.035	0.029	0.023	0.084	0.036
3DGS+SS	0.029	0.056	0.027	0.021	0.033	0.035	0.020	0.097	0.040
Mip-Splatting	0.012	0.042	0.013	0.018	0.019	0.023	0.019	0.080	0.028
Analytic-Splatting	0.013	0.043	0.013	0.020	0.021	0.027	0.023	0.079	0.030
Gaussian Blending	0.008	0.034	0.006	0.013	0.010	0.019	0.006	0.067	0.020

Table 18: Single-scale training ($\times 1/2$ resolution) and multi-scale testing results on the multi-scale Blender dataset. The best results are highlighted in **bold**.

	chair	drums	ficus	hotdog	lego	materials	mic	ship	Avg.
TensoRF	33.74	25.99	31.27	35.94	32.80	28.93	32.75	30.22	31.45
3DGS	28.18	22.34	26.81	30.17	26.34	24.29	25.88	24.79	26.10
Scaffold-GS	28.28	22.10	25.76	30.77	25.96	24.35	25.29	24.17	25.84
2DGS	24.62	22.14	27.39	29.99	25.83	24.44	25.62	24.82	25.61
3D-HGS	28.60	22.51	26.91	30.55	26.56	24.60	26.23	24.84	26.35
Tri-MipRF	32.81	24.41	29.22	35.11	31.32	28.74	31.42	28.07	30.14
3DGS+EWA	33.46	25.70	31.81	33.95	30.26	27.99	28.90	28.21	30.03
3DGS+SS	31.36	24.81	30.61	33.91	30.39	27.44	30.04	27.49	29.51
Mip-Splatting	35.44	26.52	32.69	36.21	33.02	30.29	32.15	30.03	32.04
Analytic-Splatting	35.62	26.30	33.62	36.28	33.14	29.68	32.09	30.27	32.13
Gaussian Blending	38.65	27.90	36.70	39.89	36.89	32.24	37.30	32.49	35.26
	chair	drums	ficus	hotdog	lego	materials	mic	ship	Avg.
TensoRF	0.979	0.943	0.979	0.983	0.977	0.963	0.984	0.917	0.966
3DGS	0.932	0.884	0.941	0.946	0.909	0.910	0.931	0.860	0.914
Scaffold-GS	0.936	0.878	0.933	0.957	0.910	0.912	0.927	0.851	0.913
2DGS	0.905	0.868	0.932	0.934	0.892	0.897	0.913	0.845	0.898
3D-HGS	0.935	0.886	0.940	0.950	0.913	0.914	0.936	0.861	0.917
Tri-MipRF	0.977	0.917	0.968	0.979	0.966	0.958	0.978	0.890	0.954
3DGS+EWA	0.979	0.948	0.982	0.979	0.968	0.962	0.972	0.917	0.963
3DGS+SS	0.971	0.936	0.972	0.979	0.965	0.956	0.975	0.903	0.957
Mip-Splatting	0.986	0.955	0.986	0.987	0.983	0.975	0.985	0.922	0.972
Analytic-Splatting	0.987	0.953	0.987	0.987	0.982	0.971	0.986	0.927	0.972
Gaussian Blending	0.990	0.962	0.992	0.991	0.989	0.977	0.993	0.933	0.978
	chair	drums	ficus	hotdog	lego	materials	mic	ship	Avg.
TensoRF	0.034	0.071	0.035	0.033	0.033	0.062	0.033	0.096	0.049
3DGS	0.040	0.077	0.044	0.036	0.059	0.052	0.041	0.112	0.058
Scaffold-GS	0.043	0.089	0.052	0.036	0.064	0.052	0.045	0.123	0.063
2DGS	0.089	0.099	0.053	0.047	0.075	0.058	0.054	0.126	0.075
3D-HGS	0.039	0.077	0.044	0.034	0.056	0.050	0.038	0.111	0.056
Tri-MipRF	0.032	0.093	0.043	0.032	0.040	0.056	0.029	0.120	0.056
3DGS+EWA	0.024	0.053	0.021	0.025	0.036	0.033	0.022	0.086	0.037
3DGS+SS	0.024	0.051	0.024	0.020	0.030	0.034	0.018	0.088	0.036
Mip-Splatting	0.017	0.044	0.014	0.019	0.022	0.025	0.018	0.083	0.030
Analytic-Splatting	0.014	0.045	0.015	0.019	0.020	0.030	0.020	0.077	0.030
Gaussian Blending	0.010	0.037	0.010	0.013	0.012	0.024	0.007	0.068	0.023

Table 19: Single-scale training ($\times 1/4$ resolution) and multi-scale testing results on the multi-scale Blender dataset. The best results are highlighted in **bold**.

	chair	drums	ficus	hotdog	lego	materials	mic	ship	Avg.
TensoRF	33.45	25.48	29.92	35.36	31.48	28.64	32.39	29.84	30.82
3DGS	28.54	22.37	25.36	30.28	25.12	24.09	26.29	24.98	25.88
Scaffold-GS	28.06	21.77	24.15	30.37	24.56	23.66	25.15	23.57	25.16
2DGS	25.06	23.36	27.58	31.03	26.07	25.56	28.15	26.08	26.61
3D-HGS	29.07	22.62	25.61	30.51	25.53	24.46	26.51	25.02	26.17
Tri-MipRF	31.60	24.06	27.62	34.20	29.92	27.87	30.54	28.07	29.23
3DGS+EWA	31.99	25.39	29.56	33.01	28.42	27.09	28.70	27.59	28.97
3DGS+SS	31.84	24.57	29.00	33.61	28.97	27.03	29.88	27.56	29.06
Mip-Splatting	34.72	26.37	31.12	36.34	31.78	30.03	32.73	29.98	31.63
Analytic-Splatting	35.01	26.23	32.06	36.33	32.48	29.38	32.45	30.06	31.75
Gaussian Blending	37.05	27.24	34.23	38.84	35.27	31.20	35.91	31.65	33.92
	chair	drums	ficus	hotdog	lego	materials	mic	ship	Avg.
TensoRF	0.970	0.926	0.968	0.977	0.967	0.954	0.979	0.897	0.955
3DGS	0.935	0.897	0.944	0.951	0.899	0.915	0.944	0.861	0.918
Scaffold-GS	0.935	0.884	0.931	0.954	0.892	0.909	0.933	0.836	0.909
2DGS	0.915	0.905	0.952	0.956	0.910	0.928	0.952	0.870	0.923
3D-HGS	0.938	0.898	0.944	0.952	0.905	0.919	0.945	0.860	0.920
Tri-MipRF	0.957	0.901	0.951	0.969	0.946	0.934	0.968	0.872	0.937
3DGS+EWA	0.962	0.936	0.967	0.969	0.941	0.947	0.964	0.892	0.947
3DGS+SS	0.964	0.930	0.969	0.974	0.950	0.950	0.970	0.893	0.950
Mip-Splatting	0.976	0.947	0.975	0.983	0.971	0.968	0.981	0.911	0.964
Analytic-Splatting	0.978	0.944	0.978	0.983	0.973	0.961	0.981	0.904	0.963
Gaussian Blending	0.980	0.949	0.983	0.986	0.980	0.966	0.985	0.913	0.968
	chair	drums	ficus	hotdog	lego	materials	mic	ship	Avg.
TensoRF	0.045	0.101	0.050	0.046	0.052	0.075	0.036	0.111	0.064
3DGS	0.045	0.077	0.043	0.042	0.077	0.062	0.041	0.118	0.063
Scaffold-GS	0.052	0.098	0.058	0.045	0.085	0.068	0.050	0.134	0.074
2DGS	0.096	0.091	0.046	0.046	0.082	0.059	0.043	0.125	0.074
3D-HGS	0.044	0.080	0.044	0.041	0.076	0.061	0.040	0.118	0.063
Tri-MipRF	0.057	0.122	0.069	0.057	0.069	0.090	0.051	0.133	0.081
3DGS+EWA	0.038	0.068	0.038	0.041	0.062	0.052	0.035	0.106	0.055
3DGS+SS	0.029	0.057	0.027	0.027	0.044	0.045	0.024	0.096	0.043
Mip-Splatting	0.032	0.059	0.026	0.028	0.042	0.035	0.024	0.098	0.043
Analytic-Splatting	0.024	0.060	0.030	0.027	0.034	0.049	0.025	0.092	0.043
Gaussian Blending	0.021	0.057	0.024	0.023	0.025	0.043	0.019	0.082	0.037

Table 20: Single-scale training ($\times 1/8$ resolution) and multi-scale testing results on the multi-scale Blender dataset. The best results are highlighted in **bold**.

	chair	drums	ficus	hotdog	lego	materials	mic	ship	Avg.
	PSNR \uparrow								
	chair	drums	ficus	hotdog	lego	materials	mic	ship	Avg.
TensoRF	31.22	24.14	26.79	32.89	28.38	26.87	29.50	27.97	28.47
3DGS	26.93	21.20	22.96	28.81	22.64	22.23	24.91	23.24	24.11
Scaffold-GS	25.41	19.70	21.47	28.18	21.22	20.81	22.31	19.87	22.37
2DGS	25.60	23.17	25.58	29.92	24.72	24.67	27.81	26.05	25.94
3D-HGS	27.46	21.39	23.25	28.88	23.21	22.60	24.83	23.39	24.38
Tri-MipRF	28.06	22.25	23.65	31.42	26.03	24.56	28.34	25.01	26.17
3DGS+EWA	28.91	23.59	26.52	30.55	25.39	24.59	26.64	25.56	26.47
3DGS+SS	29.94	22.90	25.56	31.27	25.83	24.63	27.62	25.72	26.68
Mip-Splatting	32.46	25.04	28.07	34.58	29.13	27.96	31.72	28.16	29.64
Analytic-Splatting	32.95	24.79	28.55	34.72	29.66	27.44	31.52	26.56	29.52
Gaussian Blending	34.21	25.47	30.07	36.08	31.28	28.66	33.35	29.19	31.04
	SSIM \uparrow								
	chair	drums	ficus	hotdog	lego	materials	mic	ship	Avg.
TensoRF	0.946	0.894	0.934	0.958	0.920	0.925	0.960	0.861	0.925
3DGS	0.908	0.871	0.916	0.929	0.848	0.874	0.932	0.810	0.886
Scaffold-GS	0.899	0.841	0.898	0.924	0.830	0.849	0.911	0.742	0.862
2DGS	0.909	0.895	0.926	0.947	0.885	0.909	0.956	0.846	0.909
3D-HGS	0.911	0.867	0.916	0.929	0.854	0.876	0.931	0.812	0.887
Tri-MipRF	0.897	0.838	0.870	0.933	0.871	0.868	0.934	0.783	0.874
3DGS+EWA	0.925	0.896	0.934	0.938	0.884	0.904	0.939	0.834	0.907
3DGS+SS	0.935	0.893	0.940	0.951	0.893	0.908	0.948	0.845	0.914
Mip-Splatting	0.954	0.918	0.945	0.970	0.932	0.944	0.969	0.879	0.939
Analytic-Splatting	0.956	0.912	0.951	0.967	0.934	0.931	0.968	0.843	0.933
Gaussian Blending	0.962	0.919	0.960	0.972	0.946	0.940	0.973	0.871	0.943
	LPIPS \downarrow								
	chair	drums	ficus	hotdog	lego	materials	mic	ship	Avg.
TensoRF	0.075	0.135	0.082	0.074	0.098	0.109	0.065	0.156	0.099
3DGS	0.074	0.111	0.068	0.074	0.124	0.100	0.059	0.164	0.097
Scaffold-GS	0.088	0.151	0.098	0.084	0.140	0.126	0.083	0.201	0.121
2DGS	0.115	0.120	0.077	0.071	0.126	0.099	0.063	0.163	0.104
3D-HGS	0.076	0.118	0.069	0.077	0.126	0.104	0.062	0.166	0.100
Tri-MipRF	0.161	0.208	0.180	0.122	0.146	0.165	0.118	0.231	0.166
3DGS+EWA	0.123	0.119	0.069	0.123	0.137	0.134	0.159	0.195	0.132
3DGS+SS	0.052	0.089	0.049	0.054	0.088	0.081	0.045	0.137	0.074
Mip-Splatting	0.072	0.100	0.066	0.071	0.100	0.066	0.053	0.147	0.084
Analytic-Splatting	0.046	0.103	0.058	0.055	0.074	0.087	0.048	0.142	0.077
Gaussian Blending	0.042	0.099	0.051	0.049	0.065	0.080	0.045	0.124	0.069

Table 21: Multi-scale training and multi-scale testing results on the multi-scale Blender dataset. The best results are highlighted in **bold**.

	chair	drums	ficus	hotdog	lego	materials	mic	ship	Avg.
	PSNR ↑								
TensoRF	33.28	25.86	31.94	35.59	32.54	29.14	32.31	29.74	31.30
3DGS	32.92	25.20	29.27	35.20	28.65	26.92	31.52	28.71	29.80
Scaffold-GS	31.35	24.38	26.29	33.69	28.28	26.08	29.73	28.01	28.48
2DGS	26.37	24.70	28.77	34.01	28.49	26.92	30.48	28.05	28.47
3D-HGS	34.45	25.89	29.78	36.41	30.89	28.36	32.79	29.35	30.99
Tri-MipRF	37.51	27.26	33.17	38.83	35.95	31.48	37.13	32.83	34.27
3DGS+EWA	34.55	26.36	32.37	36.34	31.55	29.17	31.96	29.84	31.52
3DGS+SS	36.18	26.90	32.76	37.89	33.01	29.85	34.50	31.01	32.76
Mip-Splatting	38.10	27.71	34.91	39.37	35.49	31.79	37.52	32.88	34.72
Analytic-Splatting	39.02	27.84	36.01	39.57	35.88	31.53	37.41	33.28	35.07
Gaussian Blending	40.10	28.35	37.70	40.37	37.86	32.68	38.83	33.63	36.19
	SSIM ↑								
	chair	drums	ficus	hotdog	lego	materials	mic	ship	Avg.
TensoRF	0.978	0.943	0.982	0.983	0.976	0.966	0.984	0.916	0.966
3DGS	0.979	0.940	0.965	0.983	0.958	0.955	0.981	0.916	0.960
Scaffold-GS	0.970	0.927	0.940	0.977	0.953	0.945	0.974	0.901	0.948
2DGS	0.941	0.931	0.958	0.977	0.955	0.949	0.975	0.903	0.949
3D-HGS	0.984	0.946	0.969	0.986	0.973	0.965	0.985	0.920	0.966
Tri-MipRF	0.991	0.951	0.985	0.988	0.986	0.969	0.991	0.930	0.974
3DGS+EWA	0.981	0.951	0.983	0.986	0.975	0.968	0.985	0.919	0.968
3DGS+SS	0.990	0.957	0.984	0.989	0.983	0.973	0.989	0.930	0.974
Mip-Splatting	0.992	0.963	0.991	0.991	0.988	0.978	0.994	0.932	0.979
Analytic-Splatting	0.993	0.963	0.992	0.991	0.989	0.978	0.994	0.937	0.980
Gaussian Blending	0.994	0.965	0.994	0.991	0.991	0.979	0.995	0.938	0.981
	LPIPS ↑								
	chair	drums	ficus	hotdog	lego	materials	mic	ship	Avg.
TensoRF	0.035	0.070	0.027	0.034	0.034	0.055	0.036	0.102	0.049
3DGS	0.024	0.058	0.032	0.022	0.045	0.042	0.022	0.092	0.042
Scaffold-GS	0.037	0.079	0.062	0.033	0.054	0.058	0.034	0.111	0.058
2DGS	0.086	0.079	0.044	0.043	0.061	0.053	0.038	0.116	0.065
3D-HGS	0.018	0.053	0.029	0.019	0.030	0.037	0.017	0.087	0.036
Tri-MipRF	0.014	0.055	0.019	0.018	0.015	0.040	0.013	0.080	0.032
3DGS+EWA	0.028	0.055	0.022	0.023	0.036	0.038	0.022	0.097	0.040
3DGS+SS	0.013	0.042	0.016	0.016	0.019	0.027	0.010	0.077	0.027
Mip-Splatting	0.010	0.036	0.010	0.014	0.013	0.022	0.006	0.071	0.023
Analytic-Splatting	0.008	0.036	0.008	0.013	0.012	0.023	0.007	0.068	0.022
Gaussian Blending	0.008	0.034	0.006	0.014	0.010	0.021	0.006	0.067	0.021

Table 22: Single-scale training ($\times 1$ resolution) and multi-scale testing results on the multi-scale Mip-NeRF 360 dataset. The best results are highlighted in **bold**.

	bicycle	flowers	garden	stump	treehill	room	counter	kitchen	bonsai	Avg.
3DGS	20.91	19.30	21.96	22.88	21.27	28.00	25.92	26.38	26.49	23.68
Scaffold-GS	21.74	19.79	22.82	23.40	22.04	27.43	25.71	25.80	26.15	23.87
2DGS	20.63	18.76	21.71	22.58	21.53	26.79	25.22	25.32	26.62	23.24
3D-HGS	20.83	19.34	22.16	22.87	21.45	28.39	26.41	26.58	27.24	23.92
3DGS+EWA	25.46	24.30	27.59	27.73	24.83	31.03	28.70	30.51	30.73	27.87
3DGS+SS	22.65	21.16	23.91	24.94	22.44	30.53	28.14	29.28	29.70	25.86
Mip-Splatting	26.34	24.61	28.77	28.40	24.54	31.59	29.14	31.25	31.58	28.47
Analytic-Splatting	25.93	24.26	28.31	27.55	24.64	31.49	29.11	31.13	31.62	28.23
Gaussian Blending	27.48	25.65	29.62	28.88	24.88	32.20	29.50	31.86	32.43	29.17
	bicycle	flowers	garden	stump	treehill	room	counter	kitchen	bonsai	Avg.
3DGS	0.625	0.566	0.668	0.641	0.610	0.879	0.846	0.838	0.869	0.727
Scaffold-GS	0.633	0.565	0.682	0.643	0.623	0.869	0.841	0.834	0.860	0.728
2DGS	0.572	0.523	0.625	0.600	0.591	0.846	0.816	0.798	0.844	0.690
3D-HGS	0.627	0.579	0.671	0.652	0.612	0.885	0.855	0.843	0.881	0.734
3DGS+EWA	0.818	0.737	0.885	0.823	0.758	0.940	0.918	0.926	0.941	0.861
3DGS+SS	0.730	0.671	0.790	0.759	0.686	0.931	0.911	0.927	0.936	0.816
Mip-Splatting	0.858	0.771	0.915	0.852	0.751	0.946	0.929	0.943	0.956	0.880
Analytic-Splatting	0.833	0.743	0.905	0.827	0.750	0.943	0.926	0.943	0.954	0.869
Gaussian Blending	0.869	0.784	0.925	0.859	0.764	0.952	0.933	0.954	0.958	0.889
	bicycle	flowers	garden	stump	treehill	room	counter	kitchen	bonsai	Avg.
3DGS	0.277	0.338	0.208	0.294	0.349	0.201	0.184	0.148	0.176	0.242
Scaffold-GS	0.275	0.348	0.201	0.294	0.340	0.208	0.193	0.151	0.180	0.243
2DGS	0.341	0.382	0.251	0.328	0.384	0.255	0.223	0.181	0.206	0.283
3D-HGS	0.266	0.328	0.203	0.280	0.334	0.191	0.176	0.144	0.166	0.232
3DGS+EWA	0.181	0.260	0.107	0.200	0.278	0.163	0.151	0.107	0.143	0.177
3DGS+SS	0.222	0.283	0.149	0.230	0.306	0.168	0.151	0.101	0.138	0.194
Mip-Splatting	0.121	0.178	0.069	0.144	0.211	0.150	0.134	0.086	0.119	0.135
Analytic-Splatting	0.158	0.239	0.079	0.176	0.254	0.162	0.145	0.087	0.130	0.159
Gaussian Blending	0.116	0.203	0.062	0.138	0.228	0.145	0.135	0.077	0.126	0.137

Table 23: Single-scale training ($\times 1/2$ resolution) and multi-scale testing results on the multi-scale Mip-NeRF 360 dataset. The best results are highlighted in **bold**.

	bicycle	flowers	garden	stump	treehill	room	counter	kitchen	bonsai	Avg.
3DGS	22.17	20.30	23.49	23.71	21.69	28.92	26.54	26.68	27.12	24.51
Scaffold-GS	22.98	20.57	24.51	23.98	22.93	28.54	26.38	25.96	26.62	24.72
2DGS	22.71	20.32	24.03	24.14	22.30	28.12	26.09	26.32	27.35	24.60
3D-HGS	22.41	20.46	23.96	23.78	21.99	29.32	27.11	26.56	27.75	24.82
3DGS+EWA	25.60	24.23	27.33	27.54	24.74	31.32	28.94	30.13	31.37	27.91
3DGS+SS	23.82	21.88	25.26	25.42	22.58	30.93	28.62	29.61	30.03	26.46
Mip-Splatting	26.52	24.45	28.68	28.17	24.57	31.82	29.76	31.61	32.03	28.62
Analytic-Splatting	26.15	24.54	28.48	27.60	24.42	31.83	29.55	31.70	32.06	28.48
Gaussian Blending	27.78	25.62	29.68	28.73	25.05	32.29	29.97	32.16	32.59	29.32
	bicycle	flowers	garden	stump	treehill	room	counter	kitchen	bonsai	Avg.
3DGS	0.690	0.621	0.750	0.686	0.650	0.902	0.867	0.863	0.883	0.768
Scaffold-GS	0.688	0.608	0.754	0.684	0.664	0.894	0.862	0.860	0.873	0.765
2DGS	0.665	0.591	0.724	0.663	0.641	0.877	0.847	0.828	0.864	0.744
3D-HGS	0.694	0.629	0.755	0.690	0.650	0.907	0.875	0.868	0.893	0.773
3DGS+EWA	0.807	0.734	0.864	0.809	0.754	0.940	0.917	0.921	0.944	0.855
3DGS+SS	0.763	0.696	0.832	0.767	0.700	0.937	0.916	0.930	0.939	0.831
Mip-Splatting	0.845	0.760	0.902	0.835	0.748	0.945	0.931	0.945	0.955	0.874
Analytic-Splatting	0.824	0.744	0.892	0.807	0.738	0.943	0.927	0.943	0.953	0.864
Gaussian Blending	0.864	0.782	0.916	0.851	0.764	0.951	0.937	0.955	0.962	0.887
	bicycle	flowers	garden	stump	treehill	room	counter	kitchen	bonsai	Avg.
3DGS	0.245	0.312	0.181	0.278	0.321	0.186	0.175	0.136	0.166	0.222
Scaffold-GS	0.251	0.329	0.174	0.285	0.318	0.190	0.182	0.140	0.173	0.227
2DGS	0.274	0.346	0.210	0.297	0.345	0.220	0.201	0.172	0.191	0.251
3D-HGS	0.235	0.303	0.173	0.268	0.309	0.177	0.166	0.131	0.157	0.213
3DGS+EWA	0.198	0.265	0.142	0.218	0.285	0.166	0.155	0.115	0.140	0.187
3DGS+SS	0.204	0.269	0.137	0.229	0.290	0.163	0.147	0.098	0.133	0.185
Mip-Splatting	0.139	0.193	0.089	0.164	0.228	0.151	0.133	0.084	0.116	0.144
Analytic-Splatting	0.160	0.234	0.097	0.193	0.251	0.159	0.141	0.088	0.128	0.161
Gaussian Blending	0.123	0.200	0.078	0.149	0.215	0.140	0.126	0.074	0.113	0.136

Table 24: Single-scale training ($\times 1/4$ resolution) and multi-scale testing results on the multi-scale Mip-NeRF 360 dataset. The best results are highlighted in **bold**.

	bicycle	flowers	garden	stump	treehill	room	counter	kitchen	bonsai	Avg.
3DGS	22.62	20.21	24.01	23.21	20.98	28.85	26.07	24.85	26.49	24.14
Scaffold-GS	23.04	20.70	24.26	23.76	22.48	28.21	25.74	24.74	26.03	24.33
2DGS	23.89	21.20	24.94	24.54	22.35	29.27	26.89	26.42	27.58	25.23
3D-HGS	22.96	20.56	24.65	23.58	21.69	29.45	26.63	25.18	27.32	24.67
3DGS+EWA	24.96	23.20	26.18	25.62	24.13	30.55	28.04	28.05	29.66	26.71
3DGS+SS	24.27	21.89	25.66	25.06	22.01	31.10	28.32	28.32	29.21	26.20
Mip-Splatting	26.38	24.42	27.94	27.50	24.91	32.12	29.42	31.44	32.11	28.47
Analytic-Splatting	25.78	23.87	27.94	26.79	24.00	31.88	29.30	31.24	31.46	28.03
Gaussian Blending	27.11	24.76	29.00	28.05	25.14	32.35	29.50	31.41	31.93	28.80
	bicycle	flowers	garden	stump	treehill	room	counter	kitchen	bonsai	Avg.
3DGS	0.680	0.608	0.738	0.658	0.649	0.903	0.856	0.837	0.868	0.755
Scaffold-GS	0.673	0.594	0.730	0.653	0.656	0.897	0.848	0.835	0.861	0.750
2DGS	0.689	0.612	0.740	0.669	0.658	0.904	0.868	0.838	0.883	0.762
3D-HGS	0.686	0.615	0.742	0.665	0.652	0.909	0.863	0.848	0.880	0.762
3DGS+EWA	0.736	0.675	0.784	0.714	0.703	0.918	0.879	0.859	0.909	0.797
3DGS+SS	0.742	0.673	0.807	0.729	0.689	0.933	0.901	0.908	0.925	0.812
Mip-Splatting	0.786	0.719	0.838	0.789	0.726	0.939	0.915	0.933	0.949	0.844
Analytic-Splatting	0.759	0.694	0.835	0.744	0.695	0.933	0.907	0.920	0.939	0.825
Gaussian Blending	0.811	0.741	0.863	0.809	0.744	0.947	0.923	0.938	0.953	0.859
	bicycle	flowers	garden	stump	treehill	room	counter	kitchen	bonsai	Avg.
3DGS	0.273	0.327	0.221	0.306	0.346	0.198	0.197	0.174	0.193	0.248
Scaffold-GS	0.278	0.341	0.213	0.319	0.336	0.199	0.212	0.182	0.200	0.253
2DGS	0.287	0.345	0.233	0.314	0.360	0.214	0.203	0.200	0.195	0.261
3D-HGS	0.263	0.315	0.210	0.295	0.334	0.188	0.190	0.166	0.183	0.238
3DGS+EWA	0.257	0.306	0.212	0.288	0.337	0.198	0.195	0.169	0.180	0.238
3DGS+SS	0.235	0.284	0.179	0.263	0.319	0.174	0.167	0.128	0.153	0.211
Mip-Splatting	0.204	0.245	0.160	0.216	0.282	0.165	0.157	0.107	0.130	0.185
Analytic-Splatting	0.218	0.263	0.160	0.240	0.298	0.181	0.169	0.124	0.159	0.201
Gaussian Blending	0.185	0.235	0.140	0.200	0.267	0.152	0.146	0.101	0.126	0.173

Table 25: Single-scale training ($\times 1/8$ resolution) and multi-scale testing results on the multi-scale Mip-NeRF 360 dataset. The best results are highlighted in **bold**.

	bicycle	flowers	garden	stump	treehill	room	counter	kitchen	bonsai	Avg.
3DGS	21.47	18.63	22.74	21.38	18.57	26.61	23.93	23.20	23.72	22.25
Scaffold-GS	21.54	19.25	21.56	22.15	19.70	25.75	23.38	22.65	23.29	22.14
2DGS	22.68	20.40	23.56	22.72	20.70	28.84	25.81	25.22	25.89	23.98
3D-HGS	21.95	19.30	23.01	22.07	19.74	27.26	24.61	24.06	25.24	23.03
3DGS+EWA	22.81	21.08	23.10	22.46	21.86	28.00	25.72	25.41	26.26	24.08
3DGS+SS	23.10	20.36	24.57	23.39	20.01	29.11	26.38	25.93	26.98	24.42
Mip-Splatting	25.29	23.24	26.73	26.12	24.47	30.96	28.20	29.27	30.08	27.15
Analytic-Splatting	24.29	22.10	26.00	25.08	22.73	30.62	27.81	28.80	29.61	26.34
Gaussian Blending	25.58	23.58	27.03	26.27	24.71	31.17	28.49	29.94	30.45	27.47
	bicycle	flowers	garden	stump	treehill	room	counter	kitchen	bonsai	Avg.
3DGS	0.586	0.496	0.618	0.532	0.581	0.843	0.764	0.715	0.770	0.656
Scaffold-GS	0.571	0.484	0.589	0.531	0.565	0.828	0.751	0.698	0.766	0.643
2DGS	0.611	0.526	0.639	0.547	0.598	0.884	0.814	0.749	0.821	0.688
3D-HGS	0.591	0.507	0.621	0.550	0.588	0.852	0.773	0.723	0.790	0.666
3DGS+EWA	0.606	0.551	0.640	0.539	0.584	0.855	0.784	0.725	0.806	0.677
3DGS+SS	0.644	0.566	0.696	0.611	0.621	0.891	0.830	0.809	0.852	0.725
Mip-Splatting	0.685	0.629	0.733	0.688	0.669	0.910	0.865	0.832	0.899	0.768
Analytic-Splatting	0.648	0.582	0.717	0.623	0.616	0.899	0.836	0.835	0.876	0.737
Gaussian Blending	0.707	0.649	0.752	0.704	0.687	0.921	0.877	0.851	0.909	0.784
	bicycle	flowers	garden	stump	treehill	room	counter	kitchen	bonsai	Avg.
3DGS	0.364	0.409	0.321	0.390	0.428	0.266	0.280	0.292	0.276	0.336
Scaffold-GS	0.366	0.422	0.324	0.402	0.416	0.279	0.308	0.305	0.289	0.346
2DGS	0.391	0.407	0.329	0.401	0.436	0.263	0.275	0.301	0.279	0.342
3D-HGS	0.353	0.396	0.310	0.378	0.417	0.255	0.278	0.289	0.270	0.327
3DGS+EWA	0.360	0.392	0.321	0.406	0.438	0.267	0.282	0.298	0.269	0.337
3DGS+SS	0.326	0.354	0.273	0.347	0.397	0.228	0.235	0.221	0.222	0.289
Mip-Splatting	0.318	0.339	0.262	0.326	0.380	0.220	0.229	0.216	0.199	0.277
Analytic-Splatting	0.322	0.333	0.260	0.329	0.389	0.238	0.246	0.223	0.233	0.286
Gaussian Blending	0.299	0.328	0.249	0.314	0.369	0.206	0.215	0.199	0.187	0.263

Table 26: Multi-scale training and multi-scale testing results on the multi-scale Mip-NeRF 360 dataset. The best results are highlighted in **bold**.

	bicycle	flowers	garden	stump	treehill	room	counter	kitchen	bonsai	Avg.
3DGS	25.75	23.22	27.66	26.92	24.48	31.21	28.52	30.43	29.78	27.55
Scaffold-GS	25.54	22.77	27.74	26.78	24.89	31.06	28.50	29.98	30.27	27.50
2DGS	25.23	22.11	26.89	25.68	24.31	30.75	27.93	26.96	30.13	26.67
3D-HGS	26.39	23.75	28.81	27.49	24.84	32.44	29.62	31.46	32.26	28.56
3DGS+EWA	25.79	24.00	27.47	27.28	25.06	31.75	29.37	30.75	31.51	28.11
3DGS+SS	26.91	24.47	28.86	28.17	25.08	32.12	29.56	31.67	32.01	28.76
Mip-Splatting	27.57	25.10	29.36	28.75	25.16	32.48	29.86	32.58	32.44	29.25
Analytic-Splatting	27.46	25.20	29.44	28.58	25.15	32.23	29.92	31.95	32.98	29.21
Gaussian Blending	28.30	25.80	30.19	29.06	25.39	32.14	30.05	32.12	32.73	29.53
	bicycle	flowers	garden	stump	treehill	room	counter	kitchen	bonsai	Avg.
3DGS	0.797	0.702	0.879	0.791	0.744	0.940	0.914	0.935	0.939	0.849
Scaffold-GS	0.784	0.676	0.869	0.779	0.744	0.939	0.912	0.927	0.936	0.841
2DGS	0.759	0.640	0.839	0.716	0.719	0.928	0.897	0.867	0.932	0.811
3D-HGS	0.821	0.723	0.897	0.806	0.756	0.948	0.927	0.947	0.955	0.864
3DGS+EWA	0.784	0.722	0.850	0.797	0.752	0.943	0.920	0.931	0.945	0.850
3DGS+SS	0.839	0.748	0.906	0.836	0.769	0.949	0.929	0.952	0.955	0.876
Mip-Splatting	0.867	0.774	0.919	0.855	0.765	0.950	0.931	0.953	0.958	0.886
Analytic-Splatting	0.852	0.761	0.916	0.845	0.766	0.945	0.929	0.951	0.959	0.880
Gaussian Blending	0.878	0.790	0.928	0.862	0.777	0.951	0.934	0.958	0.961	0.893
	bicycle	flowers	garden	stump	treehill	room	counter	kitchen	bonsai	Avg.
3DGS	0.211	0.286	0.121	0.224	0.299	0.166	0.157	0.102	0.144	0.190
Scaffold-GS	0.224	0.310	0.130	0.251	0.300	0.164	0.164	0.113	0.153	0.201
2DGS	0.256	0.349	0.169	0.315	0.345	0.200	0.190	0.187	0.163	0.242
3D-HGS	0.182	0.266	0.101	0.205	0.273	0.154	0.144	0.088	0.129	0.171
3DGS+EWA	0.222	0.278	0.154	0.235	0.296	0.167	0.155	0.114	0.143	0.196
3DGS+SS	0.169	0.247	0.094	0.181	0.262	0.155	0.141	0.084	0.126	0.162
Mip-Splatting	0.123	0.184	0.071	0.146	0.215	0.148	0.134	0.080	0.117	0.135
Analytic-Splatting	0.147	0.225	0.076	0.160	0.244	0.160	0.141	0.083	0.123	0.151
Gaussian Blending	0.110	0.192	0.059	0.138	0.208	0.144	0.131	0.073	0.120	0.130